

THE INTERIOR CASIMIR PROBLEM

by

SAAD ZAHEER

Submitted to the Department of Physics
in partial fulfillment of the requirements for the degree of

BACHELOR OF SCIENCE

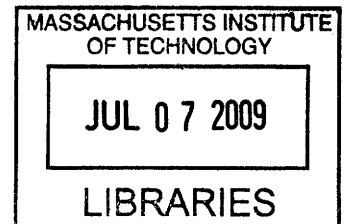
at the

MASSACHUSETTS INSTITUTE OF TECHNOLOGY

June 2009

©2009 SAAD ZAHEER
All Rights Reserved

ARCHIVES



The author hereby grants to MIT permission to reproduce and to distribute publicly
paper and electronic copies of this thesis document in whole or in part.

Author
Department of Physics
May 7, 2009

Certified by
Robert L. Jaffe
Jane and Otto Morningstar Professor of Physics
Thesis Supervisor

Accepted by
Professor David E. Pritchard
Senior Thesis Coordinator, Department of Physics

THE INTERIOR CASIMIR PROBLEM

by

SAAD ZAHEER

Submitted to the Department of Physics
on May 7, 2009, in partial fulfillment of the
requirements for the degree of
BACHELOR OF SCIENCE

Abstract

We study the electromagnetic Casimir interaction of a metallic compact object with a compact and bounded metallic surface in which it is contained. We express the interaction energy in terms of the objects' scattering matrices and *translation matrices* that relate the coordinate systems appropriate to each object. When the external conductor is a sphere and much larger than the internal conductor, the Casimir force can be expressed in terms of the static electric and magnetic multi-pole polarizabilities of the inner object, which is the interior analog of the Casimir-Polder result. Although it is not a simple power law, the dependence of the force on the separation of the object from the containing sphere is universal. Additionally, we compute the exact Casimir force between two metallic spheres contained one inside the other for arbitrary separations. Finally, we combine our results with earlier work on the Casimir force between two spheres to obtain data on the first order correction to the Proximity Force Approximation for two metallic spheres both outside and within one another.

Thesis Supervisor: Robert L. Jaffe

Title: Jane and Otto Morningstar Professor of Physics

Acknowledgments

This work was made possible in part by support from the MIT Undergraduate Research Opportunities Program. I am thankful to my collaborators, S. Jamal Rahi, Thorsten Emig and Robert L. Jaffe, for numerous useful discussions on this project, to Robert L. Jaffe for his indispensable guidance during the preparation of this thesis, and to Noah Graham and Mehran Kardar for their invaluable insights and suggestions. In the end, I am immeasurably indebted to my advisor, Professor Robert L. Jaffe, for his mentorship, advice and continued support during my undergraduate years at MIT.

Contents

| | | |
|----------|--|-----------|
| 1 | Introduction | 11 |
| 2 | Electromagnetic Field | 19 |
| 2.1 | Evaluation of the integral over sources | 20 |
| 2.2 | Numerical Results For Metallic Spheres | 24 |
| 2.3 | The Interior Casimir-Polder Result | 28 |
| 3 | Scalar Field | 33 |
| 3.1 | Interaction Energy | 33 |
| 3.2 | Numerical Results | 34 |
| 3.3 | The Scalar Interior Casimir-Polder Result | 36 |
| 4 | Corrections to the PFA | 39 |
| 5 | Conclusions | 43 |
| A | Casimir Polder Coefficient Functions: Electromagnetic Field | 45 |
| B | Casimir Polder Coefficient Functions: Scalar Field | 47 |

List of Figures

| | | |
|-----|---|----|
| 2-1 | Interior Geometry | 19 |
| 2-2 | Casimir energy between two conducting spheres | 26 |
| 2-3 | Casimir force between two conducting spheres | 27 |
| 2-4 | Interior Casimir Polder coefficients at leading order | 30 |
| 2-5 | Interior Casimir Polder coefficients at next-to-leading order | 31 |
| 2-6 | Accuracy of the interior Casimir Polder expansion | 32 |
| 3-1 | Casimir energy for a scalar field obeying Dirichlet BCs | 35 |
| 3-2 | Casimir energy for a scalar field obeying Neumann BCs | 36 |
| 3-3 | Accuracy of the scalar interior Casimir Polder expansion | 38 |
| 4-1 | Sphere-Sphere configurations | 41 |
| 4-2 | Leading order PFA corrections | 42 |

Chapter 1

Introduction

Casimir forces arise due to vacuum fluctuations of electromagnetic fields in the presence of static or slowly moving conductors, or more generally, dielectric or magnetic materials [1]. The fields obey appropriate boundary conditions on the conductors or appropriate constitutive conditions on other electromagnetically active objects, which result in induced charges and currents. Due to the quantum nature of the field, the induced charges fluctuate, shifting the energy of the vacuum by a finite amount. This difference manifests itself as an interaction — the Casimir force — between neutral objects that depends on their sizes, shapes, material properties, and relative orientations. The case of perfect conductors is particularly simple: the forces depend only on the geometry of the configuration. Analogous Casimir forces can arise from fluctuating scalar or fermion fields in the presence of objects on which they obey boundary or constitutive conditions. The electromagnetic Casimir force is a quantum effect observable at macroscopic scales. It has been shown to be significant in sub-micron scale devices as well as in the description of the interactions of atoms and/or molecules with surfaces, prompting substantial theoretical and experimental investigation over the last decade or so.

In this paper, we present the first exact calculation of the force on a small polarizable object inside a conducting spherical shell as a function of its displacement from the shell's center — the analog of the Casimir-Polder result for this geometry. We further give the first exact calculation of the force between a metallic sphere

inside a spherical shell as a function of their radii and displacement. Finally, we combine our results with earlier work on spheres [2, 3] to obtain first order corrections to the Proximity Force Approximation (PFA) for two metallic spheres both outside and within one another. This follows many attempts to calculate the Casimir force beyond PFA [4] and lends closure to this question in the case of conducting spheres.

In the past, there have not been many studies of the Casimir force in closed cavities despite the fact that cavity configurations are experimentally realizable. Dalvit *et al.* [5] studied the interaction of a cylinder inside a cylinder and recently, Marachevsky [6] has calculated the interaction of parallel plates inside a cylinder. Recent theoretical advances [2, 7] (see also Ref. [8]) in the study of the Casimir force have made it possible to analyze a wide variety of geometries and our attempt to study the interior case is one such example.

Our analysis is based on the formalism that combines path integral and scattering theory techniques, developed in Refs. [2, 9, 7]. For further references, see Ref. [7]. Based on well known scattering techniques, this method is exact for arbitrary compact objects, both conductors and dielectrics. As demonstrated in Chapters 2 and 3, the methods used in Refs. [2, 9] lend themselves very naturally to an analogous examination of our problem. In this paper, we shall not repeat formal details of the path integral method already discussed at length in Refs. [2, 9, 7, 10, 3]. Nevertheless, we summarize the formalism as it applies to conductors qualitatively to serve as a reminder for the reader. For a thorough derivation, see Ref. [7].

For a quantum field Ψ , the Casimir energy of an arbitrary configuration of objects is understood to be the difference between the vacuum energy at that configuration and at another convenient configuration where the Casimir force vanishes (in the interior problem, the force vanishes by symmetry when the objects' centers coincide if they are appropriately chosen). Formally, this can be expressed in terms of the partition function, [9]

$$\mathcal{E}[\mathcal{C}] = -\frac{\hbar c}{2\pi} \int_0^\infty d\kappa \ln \frac{\mathfrak{Z}_{\mathcal{C}}(i\kappa)}{\mathfrak{Z}_0(i\kappa)} \quad (1.1)$$

where $\mathfrak{Z}_{\mathcal{C}}(i\kappa)$, a function of imaginary frequency, is a functional of the euclidean action, [9]

$$\mathfrak{Z}_{\mathcal{C}}(i\kappa) = \int [\mathcal{D}\Psi(\mathbf{x}, i\kappa)]_{\mathcal{C}} \exp \left[-\frac{T}{\hbar} \tilde{S}[\Psi(\mathbf{x}, i\kappa)] \right] \quad (1.2)$$

The subscript \mathcal{C} denotes the spatial configuration of conductors and physically manifests itself as a boundary condition that the fluctuating field obeys on the conductors' surfaces. It is possible to trade the constraints for fluctuating sources on the constraining surfaces [2, 11]. Thus, the functional integral over the fields becomes free of constraints and can be performed up to a multiplicative constant that gets cancelled by an identical term from \mathfrak{Z}_0 . This leaves a functional integral over the fluctuating sources on the surfaces Σ_{α} , in which the action is expressed as a functional of the sources and the classical field Ψ_{cl} they produce. By superposition, we write $\Psi_{\text{cl}} = \sum_{\alpha} \Psi_{\alpha, \text{cl}}$, which allows the action to be written as a sum over the self- and inter-actions of all the objects in our system.

With the choice of convenient bases, we can expand $\Psi_{\alpha, \text{cl}}$ in terms of multipole fields, generated by the multipole moments of the sources induced on Σ_{α} . Using methods from scattering theory, we can express these multipole fields in terms of the transition matrix $\mathbb{T} = (\mathbb{S} - \mathbb{I})/2$ of the object under consideration (where \mathbb{S} is its scattering matrix) and the multipole sources. The self-action of the sources on each object can, therefore, be written entirely in terms of the multipole moments and its \mathbb{T} -matrix. Similarly, we can express the inter-action of two different objects in terms of their multipoles and a translation matrix which relates their coordinate systems in the appropriate bases. Finally, the functional integral over the multipole moments of the sources can be performed, leaving an expression for the Casimir energy in terms of the objects' \mathbb{T} matrices and the translation matrices.

We are interested in the situation in which one object, the *inner* (subscript i), is enclosed entirely within a perfect conductor, the *outer* object (subscript o). Because we take the outer object to be a perfect conductor, the presence of the inner object and its position or orientation have no effect at all on fluctuations outside the outer

object, so we may effectively ignore the space outside the inner surface of the outer object, and can therefore take the outer object to be a perfectly conducting shell of negligible thickness. The methods of Refs. [2, 9, 7] can be adapted to this *interior* problem. The polarizable inner object interacts with fields scattered *inside* as opposed to outside the outer cavity. Thus, the \mathbb{T} -matrix of the outer cavity relevant to the interior case differs from the \mathbb{T} matrix that describes scattered waves external to the outer surface. Fortunately, it turns out for a conducting cavity that the required *interior* \mathbb{T} -matrix is the just inverse of its standard (*exterior*) \mathbb{T} -matrix. Additionally, since we are interested in the fields internal to the cavity and external to the inner object, the translation matrices in the interior problem are different (\mathbb{V} instead of \mathbb{U}) from those employed in Refs. [2, 9]. With these modifications it is not surprising that, following Refs. [2, 9], Eq. (1.1) evaluates to

$$\mathcal{E}[a] = \frac{\hbar c}{2\pi} \int_0^\infty d\kappa \ln \frac{\det(\mathbb{I} - \mathbb{T}_o^{-1} \mathbb{V}_{o,i} \mathbb{T}_i \mathbb{V}_{i,o})}{\det(\mathbb{I} - \mathbb{T}_o^{-1} \mathbb{T}_i)} \quad (1.3)$$

where a denotes the displacement of centers and appears as an independent variable in the \mathbb{V} -matrices. The denominator subtracts the energy when the centers of the two objects coincide (as opposed to infinitely separated in an exterior problem [2, 9]). For further discussion, we refer the reader to Chapter 2.

The matrix identity $\ln \det \mathbb{M} = \text{Tr} \ln \mathbb{M}$, allows for a simple physical interpretation of Eq. (1.3). We can express the Casimir energy as a series, $\mathcal{E} \sim \text{Tr} (\mathbb{N} + \frac{1}{2} \mathbb{N}^2 + \dots)$, over the matrix $\mathbb{N} = \mathbb{T}_o^{-1} \mathbb{V}_{o,i} \mathbb{T}_i \mathbb{V}_{i,o}$ where \mathbb{N} describes a wave that travels from one object to the other and back [2]. In general, all terms in this series are important, illustrating the fundamentally non-two-body nature of the Casimir force. The rate of convergence of this series depends on the size of the inner object relative to the separation of its surface from that of the cavity. If the inner object is small compared to the size of the cavity, the first term in the series expansion of Eq. (1.3), $\mathcal{E} \sim \text{Tr} \mathbb{N}$, already gives an excellent approximation to the energy. Furthermore, in this limit the Casimir energy is dominated by the lowest frequency contributions from the lowest partial waves in \mathbb{T}_i . In a spherical basis, the leading terms in the electromagnetic

\mathbb{T} -matrix are, $\mathcal{T}_{lm'l'm'}^{\lambda\lambda} \sim \kappa^{l+l'+1}$ and $\mathcal{T}_{lm'l'm'}^{\lambda\sigma} \sim \kappa^{l+l'+2}$ for $\lambda \neq \sigma$. Therefore the leading contribution to the Casimir force comes from the orientation dependent response of the inner object to a dipole field, where the inner object can be characterized by its polarizability tensor, $\alpha_{mm'}^{M/E} \sim \kappa^{-3} \mathcal{T}_{1m1m'}^{M/E}$ (see Ref. [12]). The orientation dependence of the interior Casimir problem will be studied in a future publication.

The electromagnetic \mathbb{T} -matrix is diagonal for a spherically symmetric dielectric object. Therefore, for an inner sphere of radius s , the leading contributions to the Casimir force come from its static electric and magnetic polarizabilities $\alpha_1^{M,E}$. The next corrections come from its static quadrupole electric and magnetic polarizabilities, $\alpha_2^{M,E}$. This allows us to write the Casimir energy of a small dielectric sphere, not too close to the walls of a large spherical cavity, in a series in s/R , where R is the radius of the enclosing spherical shell, and the multipole polarizabilities of the small object are assumed to be of order $\alpha_\ell^{E,M} \sim s^{2\ell+1}$,

$$\frac{2\pi R}{\hbar c} \mathcal{E}(a) = \frac{\alpha_1^M}{R^3} f_M(a/R) + \frac{\alpha_1^E}{R^3} f_E(a/R) + \frac{\alpha_2^M}{R^5} g_M(a/R) + \frac{\alpha_2^E}{R^5} g_E(a/R). \quad (1.4)$$

Note that the coefficients of $1/R^p$ are non-trivial functions of a/R , where a is the distance that the small object is displaced from the center of the cavity. The underlying reason for this is that all partial waves of the cavity \mathbb{T} -matrix, \mathbb{T}_o^{-1} , contribute for all values of a/R . The expansion is asymptotic in s/R at fixed a/R .

Eq. (1.4) describes the interaction of a polarizable object (an atom for instance) inside a conducting spherical shell, which is analogous to the well-known Casimir-Polder equation [13] (and its extensions to subdominant $1/R$ dependence [2, 3]) that describes an atom's interaction with a conducting plane and with another atom. Therefore, we refer to Eq. (1.4) as the *interior Casimir-Polder* result (ICP) for the general interior problem. The Casimir force can be calculated by differentiating the ICP coefficient functions f, g with respect to a . The derivatives of the ICP coefficient functions $f'_{M/E}, g'_{M/E}$ are plotted in Figs. 2-4 and 2-5, and their functional forms are given in Appendix A.

The opposite extreme from the Casimir-Polder limit is when the interior object

is nearly touching the cavity wall. The leading behavior of the Casimir force in this limit is given by the Proximity Force Approximation [14]. The PFA prediction for the Casimir *force* between two conducting spheres, whether they are separate or one is inside the other is given by,

$$\lim_{d \rightarrow 0} d^3 \mathcal{F}(d, s, R) = -\frac{\pi^3 \hbar c}{360} \frac{sR}{R+s} \quad (1.5)$$

where s and R are the radii of the inner and outer spheres respectively and d is the minimum distance between their surfaces. By convention we keep s fixed and let R vary. $R > 0$ corresponds to the *exterior* problem, two separated spheres; $R < 0$ corresponds to the *interior* problem (see Fig. 4-1); and the $R \rightarrow \infty$ limit corresponds to a sphere opposite a plane. The constraint $|R| > s$ avoids double counting. This result is known to be exact. Ref. [16] derives the result for $R > 0$ by semi-classical methods and the extension to $R < 0$ is straightforward, but the corrections have up to now not been known. The planar and exterior problems have recently been studied in Ref. [2] and Ref. [3] respectively. Since most experiments up to now have considered spherical conductors separated by distances much smaller than their radii, the first correction in $d/R_{\text{in,out}}$ to the PFA is the geometric correction of greatest immediate interest. As discussed in Chapter 4, we parameterize the first correction to the PFA by

$$\mathcal{F}(d, s, R) \sim_{d \rightarrow 0} -\frac{\pi^3 \hbar c}{360 d^3} \frac{Rs}{R+s} \left(1 + \theta_1(s/R) \frac{d}{2s} - \theta_2(s/R) \frac{d^2}{2s^2} + \mathcal{O}(d^3/s^3) \dots \right) \quad (1.6)$$

Our analysis of the interior case has allowed us to combine our results with those of Refs. [2, 3] to predict an estimate of the PFA correction coefficient $\theta_1(s/R)$ appearing in Eq. (1.6) for $-1 \leq s/R \leq 1$. For further discussion, we refer the reader to Chapter 4.

The rest of this thesis is organized as follows: Chapter 2 begins by briefly outlining the derivation of the Casimir energy for an electromagnetic field. The vector transition and translation matrices relevant to the interior case are given, followed by

an exact computation of the Casimir force between metallic spheres in Section 2.2. In Section 2.3, we derive the interior Casimir-Polder result, and study its comparison with the exact results of Section 2.2. Chapter 3 repeats the analysis of Chapter 2 for a complex scalar field but only important results are included since they are direct analogs of the vector case. In Chapter 4, we discuss first order corrections to the Proximity Force Approximation for two metallic spheres of arbitrary size based on numerical results in this paper and in Refs. [2, 3]. After a short concluding section, the interior Casimir-Polder coefficients are given in the Appendix.

Chapter 2

Electromagnetic Field

In this chapter, we calculate the electromagnetic Casimir energy for the geometry illustrated in Fig. 2-1. We begin by briefly outlining the derivation of the action leading up to Eq. (1.3) and conclude with a detailed discussion of our results.

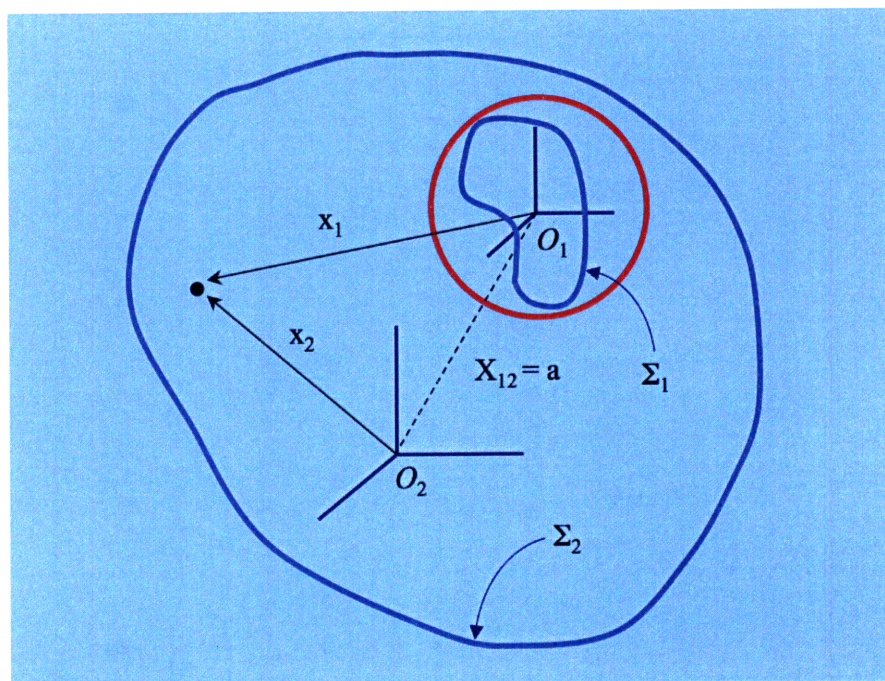


Figure 2-1: Interior Geometry: Σ_α denote the surfaces of the two objects. Σ_1 is shown with a bounding sphere. We assume that it is possible to choose a bounding sphere that does not overlap with Σ_2 . Coordinate vectors \mathbf{x}_1 and \mathbf{x}_2 to an arbitrary point are shown. The distance between the two origins is labeled $X_{12} = |\mathbf{x}_2 - \mathbf{x}_1| = a$.

2.1 Evaluation of the integral over sources

As remarked earlier, we can write the Casimir energy of a system of objects in terms of a functional integral over charges fluctuating on their surfaces. For an electromagnetic field, the fluctuating charges are the currents $\mathbf{J}_\alpha(\mathbf{x})$. Following Ref. [2], the constrained partition function for the two objects in Fig. 2-1 can be written as

$$\mathfrak{Z}_C[\mathbf{J}_1, \mathbf{J}_2] = \int [\mathcal{D}\mathbf{J}_1][\mathcal{D}\mathbf{J}_2]_C \exp(iS[\mathbf{J}_1, \mathbf{J}_2]) \quad (2.1)$$

And the electromagnetic action in terms of sources is given by, [2]

$$S[\mathbf{J}_1, \mathbf{J}_2] = \frac{1}{2} \sum_{\alpha \neq \beta} \int d\mathbf{x}_\alpha \mathbf{J}_\alpha^*(\mathbf{x}_\alpha) \frac{1}{ik} \mathbf{E}_\beta(\mathbf{x}_\alpha - \mathbf{x}_{\alpha\beta}) + \frac{1}{2} \sum_\alpha \int d\mathbf{x}_\alpha d\mathbf{x}'_\alpha \mathbf{J}_\alpha^*(\mathbf{x}_\alpha) \mathcal{G}_0(\mathbf{x}_\alpha, \mathbf{x}'_\alpha, k) \mathbf{J}_\alpha(\mathbf{x}'_\alpha) + c.c. \quad (2.2)$$

where $\mathbf{x}_{\alpha\beta} = \mathbf{x}_\alpha - \mathbf{x}_\beta$ separates the origins O_α and O_β , and \mathcal{G}_0 is the tensor Green's function for the vector Helmholtz equation with outgoing wave boundary conditions. The dependence of the fields and source on the wave number k is suppressed for simplicity. In a vector spherical basis, this Green's function is given as, [7] (we use the substitution $\kappa = -ik$ to obtain Wick-rotated formulae for this problem),

$$\begin{aligned} \mathcal{G}_0(\mathbf{x}, \mathbf{x}', \kappa) &= \kappa \sum_{lm} \left\{ \mathbf{M}_{lm}^{\text{out}}(\mathbf{x}_>) \otimes \mathbf{M}_{lm}^{*\text{reg}}(\mathbf{x}_<) + \mathbf{N}_{lm}^{\text{out}}(\mathbf{x}_>) \otimes \mathbf{N}_{lm}^{*\text{reg}}(\mathbf{x}_<) \right\} \\ &= \kappa \sum_{lm} \left\{ \mathbf{M}_{lm}^{*\text{out}}(\mathbf{x}_>) \otimes \mathbf{M}_{lm}^{\text{reg}}(\mathbf{x}_<) + \mathbf{N}_{lm}^{*\text{out}}(\mathbf{x}_>) \otimes \mathbf{N}_{lm}^{\text{reg}}(\mathbf{x}_<) \right\} \end{aligned} \quad (2.3)$$

where \mathbf{M}/\mathbf{N} denote the two polarizations of vector wave functions. The superscripts “out” and “reg” refer to the outgoing and regular solutions, which for imaginary frequency correspond to modified spherical Bessel functions, $k_\nu(\kappa r)$ and $i_\nu(\kappa r)$ respectively. Their functional forms are discussed in detail in Ref. [7]. The electric field induced on Σ_α due to $\mathbf{J}_\alpha(\mathbf{x})$ can be read off Eq. (2.2) in terms of the Green's function,

$$\mathbf{E}_\alpha(\mathbf{x}_\alpha) = -\kappa \int_{\Sigma_\alpha} d\mathbf{x}'_\alpha \mathcal{G}_0(\mathbf{x}_\alpha, \mathbf{x}'_\alpha, k) \mathbf{J}_\alpha(\mathbf{x}'_\alpha) \quad (2.4)$$

For the interior problem, we are interested in the fields external to the inner object and internal to the conducting cavity. Therefore, we expand $\mathbf{E}_1(\mathbf{x}_1)$ and $\mathbf{E}_2(\mathbf{x}_2)$ in terms of their outgoing and regular multipole fields respectively, in contrast to the exterior problem where all fields are expanded in terms of outgoing waves. Substituting the representation of \mathcal{G}_0 from Eq. (2.3) into Eq. (2.4),

$$\mathbf{E}_1(\mathbf{x}_1) = -\kappa \sum_{lm} \left\{ \mathcal{Q}_{M,lm}^1 \mathbf{M}_{lm}^{\text{out}}(\mathbf{x}_1) + \mathcal{Q}_{E,lm}^1 \mathbf{N}_{lm}^{\text{out}}(\mathbf{x}_1) \right\} \quad (2.5)$$

$$\mathbf{E}_2(\mathbf{x}_2) = -\kappa \sum_{lm} \left\{ \mathcal{Q}_{M,lm}^2 \mathbf{M}_{lm}^{\text{reg}}(\mathbf{x}_2) + \mathcal{Q}_{E,lm}^2 \mathbf{N}_{lm}^{\text{reg}}(\mathbf{x}_2) \right\} \quad (2.6)$$

where the multipole moments are defined to be,

$$\mathcal{Q}_{M,lm}^{1*} = \kappa \int_{\Sigma_1} d\mathbf{x} \mathbf{M}_{lm}^{\text{reg}}(\mathbf{x}) \mathbf{J}_1^*(\mathbf{x}), \quad \mathcal{Q}_{E,lm}^{1*} = \kappa \int_{\Sigma_1} d\mathbf{x} \mathbf{N}_{lm}^{\text{reg}}(\mathbf{x}) \mathbf{J}_1^*(\mathbf{x}) \quad (2.7)$$

$$\mathcal{Q}_{M,lm}^{2*} = \kappa \int_{\Sigma_2} d\mathbf{x} \mathbf{M}_{lm}^{\text{out}}(\mathbf{x}) \mathbf{J}_2^*(\mathbf{x}), \quad \mathcal{Q}_{E,lm}^{2*} = \kappa \int_{\Sigma_2} d\mathbf{x} \mathbf{N}_{lm}^{\text{out}}(\mathbf{x}) \mathbf{J}_2^*(\mathbf{x}) \quad (2.8)$$

Again, the definitions of \mathcal{Q}_E^2 and \mathcal{Q}_M^2 are different from those in the exterior case (see Ref. [2]).

Now, we proceed to calculate the self- and inter-action terms in Eq. (2.2). For the inter-action terms, we need to re-express the fields $\mathbf{E}_\alpha(\mathbf{x}_\alpha)$ in terms of the coordinates of Σ_β , which can be accomplished by the following translation coefficients for vector spherical waves,

$$\mathbf{M}_{lm}^{\text{reg/out}}(\mathbf{x}_\beta) = \sum_{l'm'} \left(\mathcal{B}_{l'm'lm} \mathbf{M}_{l'm'}^{\text{reg/out}}(\mathbf{x}_\alpha) - i\mathcal{C}_{l'm'lm} \mathbf{N}_{l'm'}^{\text{reg/out}}(\mathbf{x}_\alpha) \right) \quad (2.9)$$

$$\mathbf{N}_{lm}^{\text{reg/out}}(\mathbf{x}_\beta) = \sum_{l'm'} \left(\mathcal{B}_{l'm'lm} \mathbf{N}_{l'm'}^{\text{reg/out}}(\mathbf{x}_\alpha) + i\mathcal{C}_{l'm'lm} \mathbf{M}_{l'm'}^{\text{reg/out}}(\mathbf{x}_\alpha) \right) \quad (2.10)$$

Notice that in distinction to the exterior problem, we need to translate regular to regular and outgoing to outgoing waves. The translation coefficients must approach a limiting value of 1 when the two coordinate system coincide. For the geometry in Fig. (2-1) with O_1 and O_2 aligned so that they share a common z -axis, the translation

coefficients are given by, [17]

$$\begin{aligned}
\mathcal{B}_{l'm'lm}(\kappa, a) &= \delta_{mm'}(-1)^m \sqrt{\frac{(2l+1)(2l'+1)}{4ll'(l+1)(l'+1)}} \sum_{\lambda} (2\lambda+1) \begin{pmatrix} l & l' & \lambda \\ 0 & 0 & 0 \end{pmatrix} \begin{pmatrix} l & l' & \lambda \\ m & -m & 0 \end{pmatrix} \\
&\quad \times (l(l+1) + l'(l'+1) - \lambda(\lambda+1)) i_{\lambda}(\kappa a) \\
\mathcal{C}_{l'm'lm}(\kappa, a) &= \delta_{mm'} m \kappa a (-1)^m \sqrt{\frac{(2l+1)(2l'+1)}{ll'(l+1)(l'+1)}} \sum_{\lambda} (2\lambda+1) \begin{pmatrix} l & l' & \lambda \\ 0 & 0 & 0 \end{pmatrix} \begin{pmatrix} l & l' & \lambda \\ m & -m & 0 \end{pmatrix} i_{\lambda}(\kappa a)
\end{aligned} \tag{2.11}$$

Consequently, the inter-action terms are written in a compact form in terms of the multipoles \mathbb{Q}_{α} and a translation matrix \mathbb{V} as,

$$S_{\alpha\beta} = \frac{1}{2\kappa} \mathbb{Q}_{\alpha}^{\dagger} \mathbb{V} \mathbb{Q}_{\beta} + c.c. \tag{2.12}$$

where $\mathbb{Q}_{\alpha}^{\dagger} = \begin{pmatrix} \mathcal{Q}_{M,lm}^{*\alpha} & \mathcal{Q}_{E,lm}^{*\alpha} \end{pmatrix}$ and

$$\mathbb{V} = \begin{pmatrix} \mathcal{B}_{lm'l'm'} & -i\mathcal{C}_{lm'l'm'} \\ i\mathcal{C}_{lm'l'm'} & \mathcal{B}_{lm'l'm'} \end{pmatrix}$$

To calculate the self-interaction terms, $S_{\alpha\alpha}$, we need to relate the self-induced charges \mathbb{Q}_{α} to the transition matrix \mathbb{T}_{α} of the object Σ_{α} . In scattering from a surface on which a field ϕ obeys a boundary condition, the \mathbb{T} -matrix is defined as the amplitude of the outgoing wave that is generated by a scatterer in response to a specified regular solution to the wave equation. The sum of the two,

$$\phi = \phi_{\text{reg}} + \mathbb{T}\phi_{\text{out}},$$

must obey a boundary condition on surface. In the electromagnetic case ϕ is replaced by the vector field, \mathbf{E} , and the resulting \mathbb{T} -matrix has extra matrix structure due to the two polarizations of \mathbf{E} . In the present, interior configuration, a specified outgoing solution that is generated by sources on the inner object induces currents on the outer

object which, in turn give rise to a field inside the cavity that is regular at the origin of the inner object. Therefore, for a field ϕ , we are interested in solutions of the form

$$\phi = \phi_{\text{out}} + \mathbb{T}^{\text{in}} \phi_{\text{reg}}.$$

As in the exterior case the \mathbb{T}^{in} matrix is determined by the boundary condition that ϕ must obey on the surface (of the outer conductor). Comparing these two equations it is not surprising that $\mathbb{T}^{\text{in}} = \mathbb{T}^{-1}$, a result that is derived more formally in Ref. [7]. With these considerations in mind, we repeat the above procedure formally for an electromagnetic field. Recall from Eqs. (2.2) and (2.4) that we can write the self-action as

$$S_{\alpha\alpha} = -\frac{1}{2\kappa} \sum_{\alpha} \int_{\Sigma_{\alpha}} d\mathbf{x}_{\alpha} \mathbf{J}_{\alpha}^*(\mathbf{x}_{\alpha}) \mathbf{E}_{\alpha}(\mathbf{x}_{\alpha}, \kappa),$$

where we have derived \mathbf{E}_1 and \mathbf{E}_2 in terms of the “out” and “reg” solutions and their respective multipoles in Eqs. (2.5) and (2.6) respectively. We can then employ the \mathbb{T} -matrix coefficients defined above to relate the outgoing solutions of Σ_1 to its regular solutions to find for the action,

$$\begin{aligned} S_{11} &= -\frac{1}{2} \sum_{lm'l'm'} \int_{\Sigma_1} d\mathbf{x}_1 \mathbf{J}_1^*(\mathbf{x}_1) \begin{pmatrix} \mathcal{Q}_{M,lm}^1 & \mathcal{Q}_{E,lm}^1 \end{pmatrix} \mathbb{T}_{1,l'm'lm}^{-1} \begin{pmatrix} \mathbf{M}_{lm}^{\text{reg}} \\ \mathbf{N}_{lm}^{\text{reg}} \end{pmatrix} + c.c. \\ &= -\frac{1}{2\kappa} \mathbf{Q}_1^{\dagger} \mathbb{T}_1^{-1} \mathbf{Q}_1 + c.c. \end{aligned} \quad (2.13)$$

Similarly, we relate the regular solutions of Σ_2 to its outgoing solutions using the relevant \mathbb{T} -matrix coefficients as,

$$\begin{aligned} S_{22} &= -\frac{1}{2} \sum_{lm'l'm'} \int_{\Sigma_2} d\mathbf{x}_2 \mathbf{J}_2^*(\mathbf{x}_2) \begin{pmatrix} \mathcal{Q}_{M,lm}^2 & \mathcal{Q}_{E,lm}^2 \end{pmatrix} \mathbb{T}_{2,l'm'lm} \begin{pmatrix} \mathbf{M}_{lm}^{\text{out}} \\ \mathbf{N}_{lm}^{\text{out}} \end{pmatrix} + c.c. \\ &= -\frac{1}{2\kappa} \mathbf{Q}_2^{\dagger} \mathbb{T}_2 \mathbf{Q}_2 + c.c. \end{aligned} \quad (2.14)$$

where

$$\mathbb{T}_{\alpha,lm'l'm'} = \begin{pmatrix} \mathcal{T}_{\alpha,lm'l'm'}^{MM} & \mathcal{T}_{\alpha,lm'l'm'}^{NM} \\ \mathcal{T}_{\alpha,lm'l'm'}^{MN} & \mathcal{T}_{\alpha,lm'l'm'}^{NN} \end{pmatrix}$$

With Eqs. (2.12), (2.13), and (2.14) we can write Eq. (2.2) compactly as,

$$S = -\frac{1}{2\kappa} \mathbb{Q}^\dagger \mathbb{M} \mathbb{Q} + c.c. \quad (2.15)$$

where $\mathbb{Q} = \begin{pmatrix} \mathbb{Q}_1 & \mathbb{Q}_2 \end{pmatrix}$, and

$$\mathbb{M} = \begin{pmatrix} \mathbb{T}_1^{-1} & -\mathbb{V} \\ -\mathbb{V} & \mathbb{T}_2 \end{pmatrix}$$

The functional integral in Eq. (1.2) can then be performed over charges \mathbb{Q} to give for the Casimir energy,

$$\mathcal{E}[a] = \frac{\hbar c}{2\pi} \int_0^\infty d\kappa \ln \frac{\det(\mathbb{I} - \mathbb{T}_2^{-1} \mathbb{V} \mathbb{T}_1 \mathbb{V})}{\det(\mathbb{I} - \mathbb{T}_2^{-1} \mathbb{T}_1)} \quad (2.16)$$

2.2 Numerical Results For Metallic Spheres

In this section, we present results for the Casimir force and energy between a conducting sphere and a conducting spherical shell within which it is contained. The \mathbb{T} -matrix for a conducting sphere of radius R is diagonal in both l and m , and its coefficients are given in terms of modified spherical bessel functions as,

$$\begin{aligned} \mathcal{T}_{lm'l'm'}^{MM} &= \delta_{ll'} \delta_{mm'} (-1)^l \frac{i_l(\kappa R)}{k_l(\kappa R)} \\ \mathcal{T}_{lm'l'm'}^{NN} &= \delta_{ll'} \delta_{mm'} (-1)^l \frac{i_l(\kappa R) + \kappa R i_l'(\kappa R)}{k_l(\kappa R) + \kappa R k_l'(\kappa R)} \end{aligned} \quad (2.17)$$

The interaction energy of this system is obtained by numerical integration of Eq. (2.16). It depends on the ratio of the radii, s/R , and varies with the displacement of the centers, conveniently parameterized by $x = a/(R - s)$. To be specific, we choose $s/R = 0.5$ and plot the energy in Fig. 2-2. The Casimir force, plotted in Fig. 2-3, is

obtained by numerically differentiating sample points in Fig. 2-2 spaced at $\Delta x = 0.025$ along the x -axis. Since the Casimir energy grows rapidly in the limit $x \rightarrow 1$, the differentiation in this region must be performed by fitting numerical data points to a suitable function. The numerical integration and differentiation were performed with MATLAB while all fitting and extrapolation procedures were performed with GNUPLOT.

Both the Casimir force and the Casimir energy vary over many orders of magnitude as x varies from 0 to 1. In order to display our results in a compact form, we have divided both the force and the energy by an interpolating formula obtained by taking the proximity force approximation seriously for all x . For reasons discussed in Chapter 4 we call this the *full PFA* or fPFA, and the expression for $\mathcal{E}_{\text{fPFA}}$ can be found in Eq. (4.3). There is no reason to believe that this extension of the PFA gives an accurate representation of the Casimir energy or force except as $x \rightarrow 1$, and indeed our results differ from the fPFA estimate except near $x = 1$, where they approach the PFA as they should.

Although the Casimir energy gets contributions from all partial waves bouncing back back and forth between the conducting spheres, it is dominated by partial waves $l \leq l_{\text{max}}$, where l_{max} depends on the spheres' relative sizes and separation and grows rapidly as the separation gets small. It turns out, as shown by the blue curve in Fig. 2-2, that $l_{\text{max}} \leq 25$ for $x \leq 0.7$ in the case of $s/R = 0.5$. For $x > 0.7$ in this configuration, the numerical evaluation of Eq. (2.16) is limited by our ability to manipulate large matrices. For example, the Inset in Fig. 2-2 shows that $l_{\text{max}} > 65$ at $x \sim 0.9$. Therefore, we fix x in this region and integrate Eq. (2.16) at various l to obtain contributions $\mathcal{E}(l)$ and obtain the $l \rightarrow \infty$ limit by fitting the various $\mathcal{E}(l)$ to a decaying exponential (which seems to capture the leading behavior at large l) of the form $\mathcal{E}(l) = \mathcal{E}(\infty) - \alpha e^{-\beta l}$, where α and β are constants. This convergence is depicted pictorially in the Inset of Fig. 2-2.

At even closer separations, $x \geq 0.925$ in Fig. 2-2, the leading contribution to the Casimir energy comes from even larger values of l which means that the integration of Eq. (2.16) requires manipulating very large matrices. This is an extremely

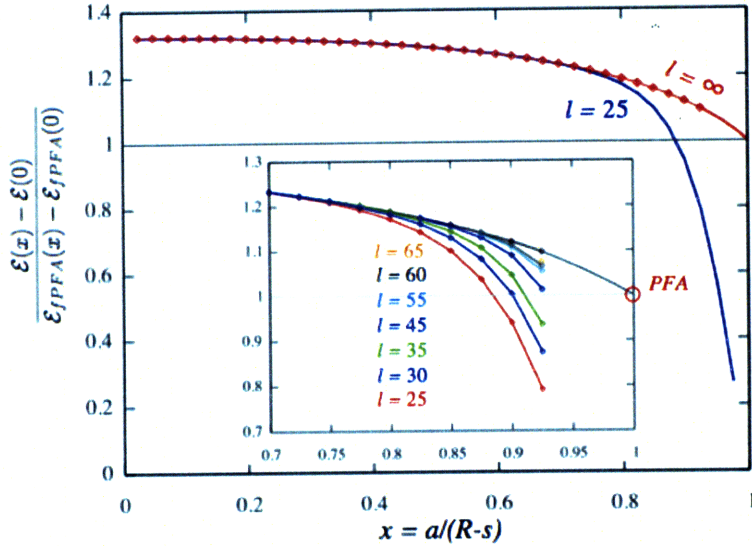


Figure 2-2: Casimir energy between two conducting spheres. The red line shows the Casimir energy, $(\mathcal{E}(x) - \mathcal{E}(0))/(\mathcal{E}_{fPFA}(x) - \mathcal{E}_{fPFA}(0))$, as a function of $x = a/(R - s)$ where a is the displacement of centers. The radius of the inner sphere is fixed at $s = 0.5R$, where R is the radius of the outer sphere. In the limit $x \rightarrow 1$, the Casimir energy approaches the PFA energy, which is marked by the gray horizontal line. \mathcal{E}_{fPFA} denotes the ‘full’ form of the PFA energy discussed in Chapter 4. At intermediate separations, the Casimir energy is dominated by lower partial waves. For example, the blue line shows that the energy obtained by integrating Eq. (2.16) to partial wave order $l = 25$ is accurate up to $x \sim 0.7$. The red line is obtained by extrapolating to $l = \infty$. Inset: Convergence at close separations, $0.7 \leq x \leq 1$.

computationally intensive problem. We are, however, remedied by the fact that the Casimir energy approaches the PFA limit as $x \rightarrow 1$. Therefore, we extrapolate from the exact data calculated at points $x \leq 0.925$ to estimate the Casimir energy for $0.925 \leq x \leq 1$. For Fig. 2-2, this was achieved by extrapolating the four data points between $0.85 \leq x \leq 0.925$ to a function, $f(d/s) = 1 + \theta_1 d/s + \theta_2 \log(d/s) d^2/s^2$, where $d = R - s - a$. Notice that the form of $f(d/s)$ corresponds to the PFA prediction for the Casimir force in Eq. (1.6). For a detailed discussion on the sub-leading contributions to the PFA, we refer the reader to Chapter 4.

The Casimir force between two conducting spheres depicted in Fig. 2-3 is calculated by numerical differentiation of the sample data points spaced at $\Delta x = 0.025$ along the red curve $R(x)$ in Fig. 2-2. We remind the reader that Fig. 2-2 plots $R(x) = (\mathcal{E}(x) - \mathcal{E}(0))/(\mathcal{E}_{fPFA}(x) - \mathcal{E}_{fPFA}(0))$ as a function of x . The curve appearing

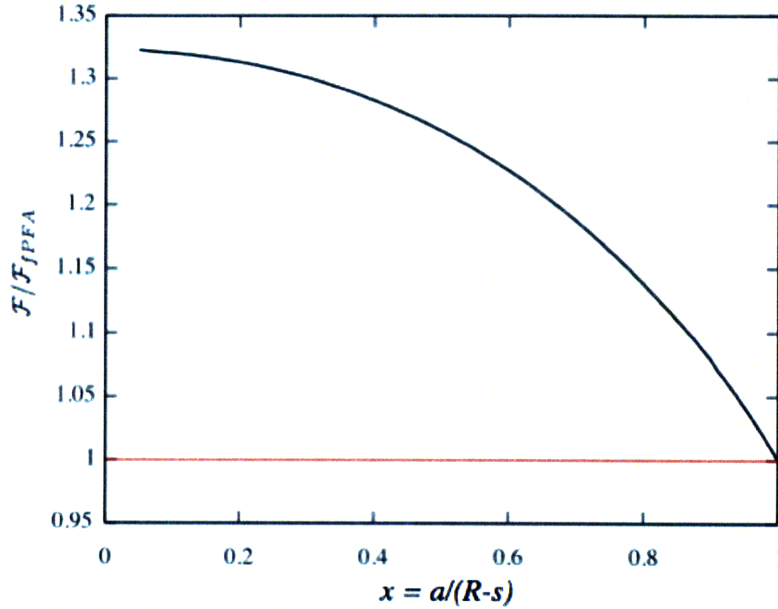


Figure 2-3: Casimir force between two conducting spheres. The black line shows the Casimir force, $\mathcal{F}/\mathcal{F}_{fPFA}$, between two conducting spheres as a function of $x = a/(R-s)$ where a is the displacement of their centers. The radius of the inner sphere is fixed at $s = 0.5R$, where R is the radius of the outer sphere. In the limit $x \rightarrow 1$, the Casimir force approaches the PFA, which is marked by the red horizontal line. \mathcal{F}_{fPFA} denotes the ‘full’ form of the PFA discussed in Chapter 4.

in Fig. 2-3 is calculated using $R(x)$ as follows,

$$\frac{\mathcal{F}(x)}{\mathcal{F}_{fPFA}(x)} = R(x) + \frac{(\mathcal{E}_{fPFA}(x) - \mathcal{E}_{fPFA}(0))}{\mathcal{F}_{fPFA}(x)} R'(x)$$

The differentiation of $R(x)$ is performed using centered differences for 35 data points between 0.05 and 0.9 with a step size of $\Delta x = 0.025$. For $x \geq 0.9$, $\mathcal{F}/\mathcal{F}_{fPFA}$ is calculated by differentiating the extrapolation function $f(d/s)$ defined above with the coefficients θ_1, θ_2 determined in Fig. 2-2. This achieves two goals: it makes contact with the PFA prediction in Eq. (1.6) and demonstrates that the function $f(d/s)$ used to extrapolate $R(x)$ at values of x close to 1 was the correct ‘ansatz’ for the sub-leading PFA behavior for the energy in Fig. 2-2.

Our discussion of the numerical results has been restricted to the case $s/R = 0.5$. However, the same techniques may be applied to determine the Casimir force and energy by numerically integrating Eq. (2.16) for all configurations, $0 < s/R < 1$.

In Chapter 4, we apply the methods demonstrated in this section to study various s/R configurations in the limit $x \rightarrow 1$ to determine the PFA correction coefficients θ_1 corresponding to those configurations. On the other hand, the Casimir force for intermediate values of a/R is studied completely analytically for the range of interior configurations $s/R \rightarrow 0$ in the following Section.

2.3 The Interior Casimir-Polder Result

In this section, we derive the Casimir energy of and Casimir force on a small polarizable object contained inside a conducting spherical shell. The matrix identity $\ln \det \mathbb{M} = \text{Tr} \ln \mathbb{M}$, allows for an expansion of the integrand in Eq. (2.16) as a series, $\mathcal{E} \sim \text{Tr} (\mathbb{N} + \frac{1}{2}\mathbb{N}^2 + \dots)$, over the matrix $\mathbb{N} = \mathbb{T}_o^{-1} \mathbb{V}_{o,i} \mathbb{T}_i \mathbb{V}_{i,o}$ where \mathbb{N} describes a wave that travels from one object to the other and back [2]. Although it is tempting to try to extract the low frequency behavior in $\text{Tr} \mathbb{N}$, we are cautioned by Eqs. (2.17) that \mathbb{T}_o^{-1} diverges at low frequencies. Instead we treat the inner sphere as a small object and expand $\text{Tr} \mathbb{N}$ in terms of the lower partial waves in \mathbb{T}_i . In a spherical basis, the leading terms in the electromagnetic \mathbb{T} -matrix are, $\mathcal{T}_{lm'l'm'}^{\lambda\lambda} \sim \kappa^{l+l'+1}$ and $\mathcal{T}_{lm'l'm'}^{\lambda\sigma} \sim \kappa^{l+l'+2}$ for $\lambda \neq \sigma$. Therefore the leading contribution to the Casimir force comes from the orientation dependent response of the inner object to a dipole field, where the inner object can be characterized by its polarizability tensor, $\alpha_{mm'}^{M/E} \sim \kappa^{-3} \mathcal{T}_{1m1m'}^{M/E}$ (see Ref. [12]). The orientation dependence of the interior Casimir problem will be studied in a future publication.

For a spherically symmetric dielectric object, the electromagnetic \mathbb{T} -matrix is diagonal in partial wave indices, l and m , and the polarizations λ . Therefore, the leading order terms in \mathbb{T}_i are characterized by the *static* magnetic and electric multipole polarizabilities $\alpha_i^{M/E}$ of the inner object [2], which can be computed or measured easily for any compact conductor. At low frequencies, the \mathbb{T} -matrix can be written

as,

$$\mathcal{T}_{lm'l'm'}^{MM} = \delta_{ll'}\delta_{mm'}\kappa^{2l} \left[\frac{(-1)^{l-1}(l+1)\alpha_l^M}{l(2l+1)!!(2l-1)!!}\kappa + \gamma_{l3}^M\kappa^3 + \gamma_{l4}^M\kappa^4 + \dots \right] \quad (2.18)$$

and $\mathcal{T}_{lm'l'm'}^{NN}$ is obtained by the substitution $\alpha_l^M \rightarrow \alpha_l^E$ and $\gamma_{ln}^M \rightarrow \gamma_{ln}^E$. Substituting Eqs. (2.17) and (2.11) in $\text{Tr } \mathbb{N}$ we find the Casimir energy up to $\mathcal{O}(R^{-5})$ to be,

$$\frac{2\pi R}{\hbar c}\mathcal{E}(a) = \frac{\alpha_1^M}{R^3}f_M(a/R) + \frac{\alpha_1^E}{R^3}f_E(a/R) + \frac{\alpha_2^M}{R^5}g_M(a/R) + \frac{\alpha_2^E}{R^5}g_E(a/R) \quad (2.19)$$

Eq. (2.19) describes the interaction of a polarizable object (an atom for instance) inside a conducting spherical shell, which is analogous to the well-known Casimir-Polder equation [13] (and its extensions to subdominant $1/R$ dependence calculated in Refs. [2, 3]) that describes an atom's interaction with a conducting plane or with another atom.

We have calculated exact functional forms of the interior Casimir-Polder coefficients f and g in terms of modified Bessel functions I_ν and K_ν . They can be expanded as a power series in a^2/R^2 which converges for $a^2/R^2 < 1$. The Casimir force can be calculated by differentiating the ICP coefficient functions f, g with respect to a . We have plotted their derivatives f', g' in Figs. 2-4 and 2-5 while their exact functional forms are given in Appendix A.

To examine the usefulness of the interior Casimir-Polder expansion, we compare the accuracy of Eq. (2.19) with the exact prediction of Eq. (2.16) for the case of an interior sphere, for which $\alpha_l^M = -l/(l+1)s^{2l+1}$ and $\alpha_l^E = s^{2l+1}$. Fig. 2-6 plots the fractional errors $\Delta\mathcal{E} = (\mathcal{E} - \mathcal{E}_{CP})/\mathcal{E}$ vs. $x = a/(R-s)$ for various s . \mathcal{E}_{CP} denotes the energy calculated using Eq. (2.19). The 1st-order data include contributions from $\mathcal{O}(R^{-3})$ terms only, while the 2nd-order data include coefficients from g_E and g_M at $\mathcal{O}(R^{-5})$ in Eq. (2.19). Many trends are visible in this graph, for example the interior Casimir-Polder result through second order differs from the exact result by less than 1 part in a 100 for all $s/R \leq 0.1$ for $0 < x < 0.34$. Another interesting feature is that for a given value of s/R , $\lim_{x \rightarrow 0} \Delta\mathcal{E}$ appears to be non-zero. Both the

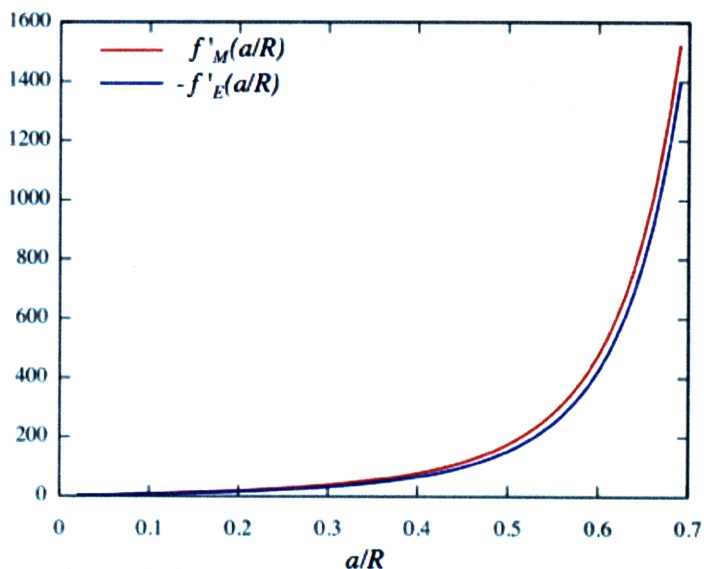


Figure 2-4: Interior Casimir-Polder coefficients for the Casimir force between dielectric spheres at leading order $\mathcal{O}(R^{-3})$. The ICP coefficient functions f_M and f_E are given in Appendix A. The derivatives f'_M and f'_E are computed by numerically differentiating f_M and f_E , which are calculated at sample points spaced at $\Delta a/R = 0.01$. The ICP coefficient functions were calculated using MATHEMATICA.

exact Casimir energy and the interior Casimir-Polder approximation vanish like a^2 as $a \rightarrow 0$ (remember the value of each at $a = 0$ has been subtracted). Notice, however, that the CP approximation is an expansion in s/R , not a/R , and therefore each term contributes, albeit with smaller magnitude, at $a = 0$. Therefore, we conclude that the ICP expansion is exact for a small polarizable object (an atom or a molecule) inside a conducting spherical shell.

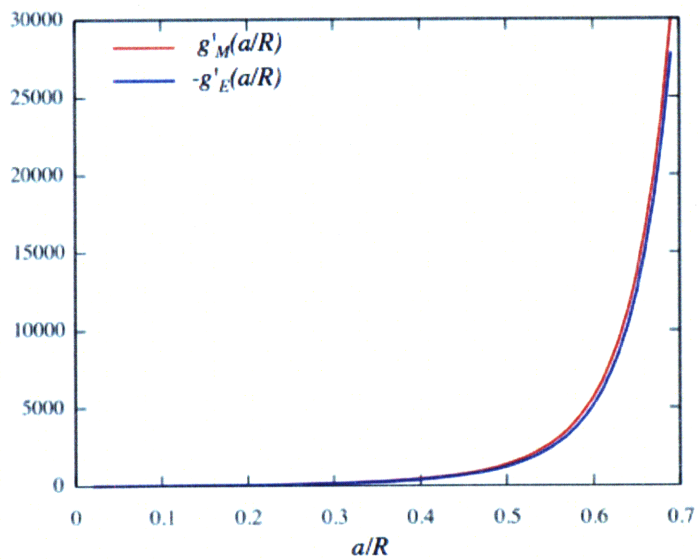


Figure 2-5: Interior Casimir-Polder coefficients for the Casimir force between dielectric spheres at next-to-leading order $\mathcal{O}(R^{-5})$. The ICP coefficient functions g_M and g_E are given in Appendix A. The derivatives g'_M and g'_E are computed by numerically differentiating g_M and g_E , which are calculated at sample points spaced at $\Delta a/R = 0.01$. The ICP coefficient functions were calculated using MATHEMATICA.

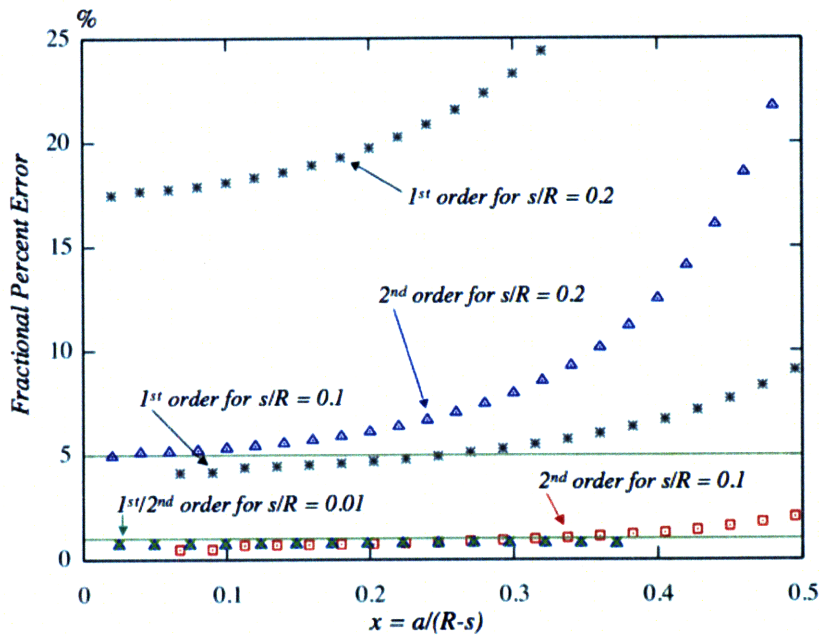


Figure 2-6: Fractional ICP comparison with the exact answer predicted by Eq. (2.16) for conducting spheres in three different configurations: $s/R = 0.2, 0.1, 0.01$. Along the y -axis is the fractional error $(\mathcal{E} - \mathcal{E}_{CP})/\mathcal{E}$ plotted as a percentage, where \mathcal{E}_{CP} is the ICP prediction from Eq. (2.19). For each value of s/R , we have plotted the fractional difference between \mathcal{E} and \mathcal{E}_{cp} at the leading order $\mathcal{O}(R^{-3})$ and next-to-leading order $\mathcal{O}(R^{-5})$. The two gray horizontal lines mark the 5% and 1% differences.

Chapter 3

Scalar Field

In this chapter, we repeat the analysis of Chapter 2 for a complex scalar field obeying Dirichlet or Neumann boundary conditions on a sphere contained inside a spherical shell. This chapter is organized on the pattern of the previous chapter, but we restrict our discussion to important results and skip formal derivations since they follow analogously from Chapter 2. The analog of the interior Casimir-Polder result for a scalar field obeying Dirichlet boundary conditions is also derived in Section 3.3.

3.1 Interaction Energy

The derivation of the interaction energy for the interior geometry in Fig. (2-1) for a complex scalar field obeying Dirichlet and Neumann boundary conditions is completely analogous to the electromagnetic case. Therefore, we include only important results which are, of course, simpler analogs of the electromagnetic case.

The translation coefficients for spherical (regular \rightarrow regular) and (outgoing \rightarrow outgoing) wave solutions to the Helmholtz equation are given as, [17] (where $\lambda = 2l + 1$),

$$\mathcal{V}_{l'm'lm}^{\alpha\beta} = \sqrt{4\pi\lambda\lambda'} i^{l-l'} (-1)^m \sum_{l''m''} i^{l''} \sqrt{\lambda''} \begin{pmatrix} l & l' & l'' \\ 0 & 0 & 0 \end{pmatrix} \begin{pmatrix} l & l' & l'' \\ m & -m' & -m'' \end{pmatrix} j_{l''}(kd_{\alpha\beta}) Y_{l''m''}(\hat{\mathbf{X}}_{\alpha\beta}) \quad (3.1)$$

The \mathbb{T} -matrix for a sphere of radius R is expressed in terms of modified spherical bessel functions i_ν and k_ν as,

$$\mathcal{T}_{lm'l'm'}^D = \delta_{ll'}\delta_{mm'}(-1)^l \frac{i_l(\kappa R)}{k_l(\kappa R)}, \quad \mathcal{T}_{lm'l'm'}^N = \delta_{ll'}\delta_{mm'}(-1)^l \frac{i_l'(\kappa R)}{k_l'(\kappa R)} \quad (3.2)$$

where D and N denote Dirichlet and Neumann boundary conditions respectively. The functional integral in Eq. (1.2) can then be performed over induced charges \mathcal{Q} to obtain for the Casimir energy,

$$\mathcal{E}[a] = \frac{\hbar c}{2\pi} \int_0^\infty d\kappa \ln \frac{\det(\mathbb{I} - \mathbb{T}_2^{-1} \mathbb{V}_{21} \mathbb{T}_1 \mathbb{V}_{12})}{\det(\mathbb{I} - \mathbb{T}_2^{-1} \mathbb{T}_1)} \quad (3.3)$$

which is analogous to Eq. (2.16) derived for the electromagnetic field in Chapter 2.

3.2 Numerical Results

In this section, we present results for the Casimir energy of a sphere inside a spherical shell for a scalar field obeying Dirichlet (DBC) or Neumann boundary conditions (NBC) on the surfaces of the spheres. The interaction energy of this system, plotted in Figs. 3-1 and 3-2, is obtained by numerical integration of Eq. (3.3) for DBCs and NBCs respectively using the relevant \mathbb{T} -matrices from Eq. (3.2). The sample points in Figs. 3-1 and 3-2 are spaced at $\Delta x = 0.025$ along the x -axis. Both Figs. 3-1 and 3-2 display the exact energy divided by the ‘full’ form of the energy, \mathcal{E}_{fPFA} , predicted by the proximity force theorem [14].

The discussion of results in this section is completely analogous to Section 2.2. For a scalar field obeying either Dirichlet or Neumann boundary conditions, the Casimir energy gets contributions from all partial waves bouncing back and forth between the two spheres. At intermediate separations, it is dominated by partial waves $l \leq l_{\max}$ where l_{\max} depends on the spheres’ relative size and separation and grows rapidly at infinitesimal separations. For $0.65 \leq x \leq 0.9$ in both Figs. 3-1 and 3-2, we truncate the matrices appearing in Eq. (3.3) at various l and obtain the $l \rightarrow \infty$ limit by fitting to a decaying exponential of the form $\mathcal{E}(l) = \mathcal{E}(\infty) - \alpha e^{-\beta l}$, where α and β

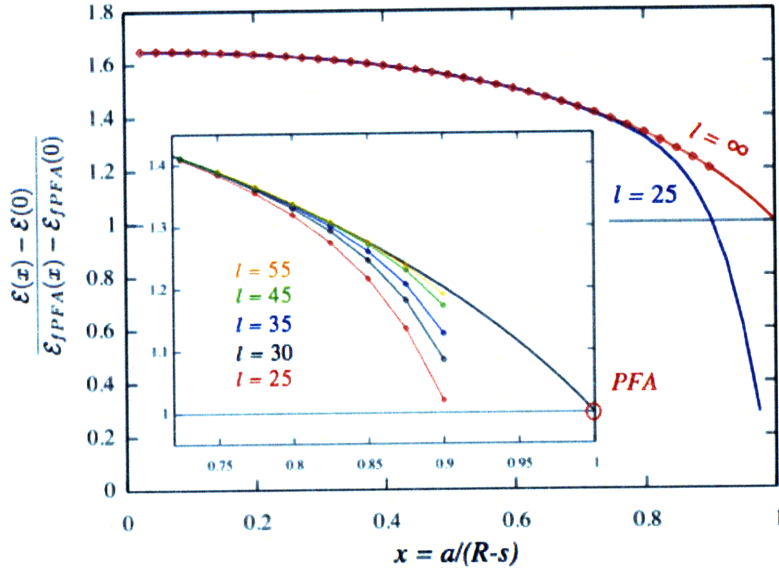


Figure 3-1: Casimir energy between two spheres for a scalar field obeying Dirichlet boundary conditions on their surfaces. The red line shows the Casimir energy, $(\mathcal{E}(x) - \mathcal{E}(0))/(\mathcal{E}_{fPFA}(x) - \mathcal{E}_{fPFA}(0))$, as a function of $x = a/(R - s)$ where a is the displacement of centers. The radius of the inner sphere is fixed at $s = 0.5R$, where R is the radius of the outer sphere. In the limit $x \rightarrow 1$, the Casimir energy approaches the PFA energy, which is marked by the gray horizontal line. \mathcal{E}_{fPFA} denotes the ‘full’ form of the PFA energy discussed in Chapter 4. At intermediate separations, the Casimir energy is dominated by lower partial waves. For example, the blue line shows that the energy obtained by integrating Eq. (3.3) for DBCs to partial wave order $l = 25$ is accurate up to $x \sim 0.65$. The red line is obtained by extrapolating to $l = \infty$. Inset: Convergence at close separations, $0.7 \leq x \leq 1$.

are constants. This convergence is also depicted in Figs. 3-1 and 3-2 for the scalar case in analogy to Fig. 2-2 for the EM case. In the limit $x \rightarrow 1$, the Casimir energy for a scalar field obeying DBCs on the two spheres is obtained by extrapolating from the six data points between $x = 0.75$ and $x = 0.9$ with a fitting function of the form, $f(d/s) = 1 + \theta_1 d/s + \theta_2 \log(d/s)d^2/s^2 + \theta_3 d^2/s^2$. Similarly, for a scalar field obeying NBCs on the spheres, the Casimir energy in the $x \rightarrow 1$ limit is obtained by extrapolating from the five data points between $x = 0.8$ and $x = 0.9$ with a fitting function of the form, $f(d/s) = 1 + \theta_1 d/s + \theta_2 \log(d/s)d^2/s^2$.

As in Section 2.2, the numerical integration of Eq. (3.3) was performed with MATLAB while all fitting and extrapolation procedures were performed with GNUPLOT.

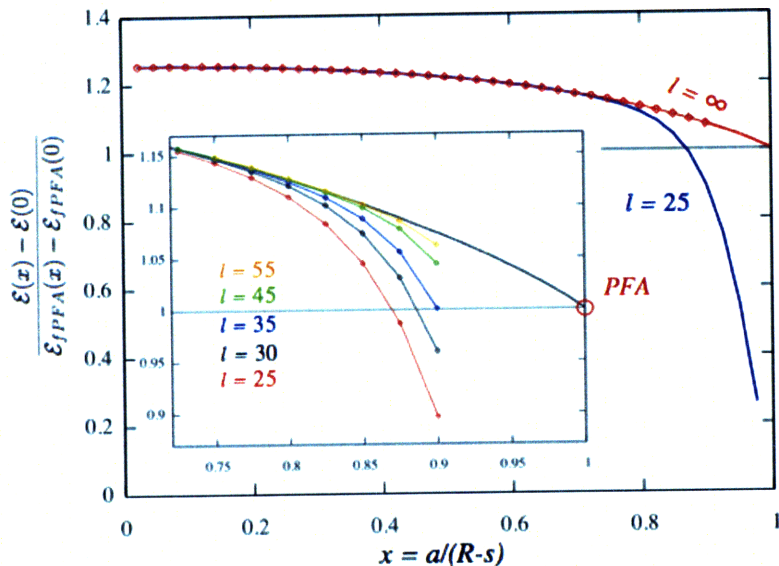


Figure 3-2: Casimir energy between two spheres for a scalar field obeying Neumann boundary conditions on their surfaces. The red line shows the Casimir energy, $(\mathcal{E}(x) - \mathcal{E}(0))/(\mathcal{E}_{fPFA}(x) - \mathcal{E}_{fPFA}(0))$, as a function of $x = a/(R - s)$ where a is the displacement of centers. The radius of the inner sphere is fixed at $s = 0.5R$, where R is the radius of the outer sphere. In the limit $x \rightarrow 1$, the Casimir energy approaches the PFA energy, which is marked by the gray horizontal line. \mathcal{E}_{fPFA} denotes the ‘full’ form of the PFA energy discussed in Chapter 4. At intermediate separations, the Casimir energy is dominated by lower partial waves. For example, the blue line shows that the energy obtained by integrating Eq. (3.3) for NBCs to partial wave order $l = 25$ is accurate up to $x \sim 0.65$. The red line is obtained by extrapolating to $l = \infty$. Inset: Convergence at close separations, $0.7 \leq x \leq 1$.

3.3 The Scalar Interior Casimir-Polder Result

In this section, we derive the analog of the interior Casimir-Polder result for a scalar field obeying Dirichlet boundary conditions on the inner surface of a spherical shell and on the outer surface of a small arbitrary shaped object. In analogy with Section 2.3, we use the matrix identity $\ln \det \mathbb{M} = \text{Tr} \ln \mathbb{M}$, to expand the integrand in Eq. (3.3) as a series over the matrix $\mathbb{N} = \mathbb{T}_o^{-1} \mathbb{V}_{o,i} \mathbb{T}_i \mathbb{V}_{i,o}$. We treat the inner sphere as a small object and expand $\text{Tr} \mathbb{N}$ in terms of the lower partial waves in \mathbb{T}_i . This allows us to treat the inner object as arbitrarily shaped because at low frequencies for Dirichlet Boundary conditions, the scalar \mathbb{T} -matrix of a compact object is related

to tensor generalizations of its capacitance, \mathcal{C} , as [9]

$$\mathcal{T}_{l'm'lm} = \frac{i^{l+l'}}{(2l+1)!!(2l-1)!!} \sum_{q=0}^{\infty} \mathcal{C}_{q;l'm'lm} \kappa^{l+l'+1+q} \quad (3.4)$$

In contrast to the electromagnetic case, where \mathbb{T} begins at $\mathcal{O}(\kappa^3)$, the scalar \mathbb{T} -matrix begins at $\mathcal{O}(\kappa)$, so higher terms in the expansion of $\text{Tr} \ln \mathbb{N}$ contribute at lower orders in the ICP expansion. $\mathcal{O}(k)$ in \mathbb{T} maps to $\mathcal{O}(1/R)$ in the expansion of $R\mathcal{E}$, so if we keep terms through $\mathcal{O}(1/R^4)$ in the Casimir energy, we will encounter contributions involving up to four “reflections”, proportional to \mathcal{C}^4 . Some special cases are, $\mathcal{C}_{0,0000} = -\mathcal{C}$, $\mathcal{C}_{1,0000} = \mathcal{C}^2$, $\mathcal{C}_{2,0000} = \mathcal{D} - \mathcal{C}^3$, $\mathcal{C}_{0,1m1m'} = \mathcal{A}_{mm'}$ where \mathcal{D} and $\mathcal{A}_{mm'}$ are the effective range and the polarizability tensor respectively. The *effective range* \mathcal{D} is related to the S-wave phase shift δ by the relation, $k \cot \delta = \mathcal{C}^{-1} - \mathcal{D}k^2/\mathcal{C}^2$, where k^2 is the energy of the wave [19]. In our normalization, the S-wave term in the \mathbb{T} -matrix can be written as, $\mathcal{T}_0 = i/(\cot \delta - i)$, which for imaginary frequency $\kappa = -ik$ becomes $\mathcal{T}_0 = -\mathcal{C}\kappa + \mathcal{C}^2\kappa^2 + (\mathcal{D} - \mathcal{C}^3)\kappa^3 + \mathcal{O}(\kappa^4)$. Additionally, we use the freedom to choose the origin of the coordinate system centered on the object so that the dipole response to a constant potential vanishes i.e. $\mathcal{C}_{0;1m00}^1 = \mathcal{C}_{0;001m}^1 = 0$.

With the assumption that $\mathcal{C}/R \ll 1$, we can expand Eq. (3.3) in powers of \mathcal{C}/R as,

$$\begin{aligned} \frac{2\pi R}{\hbar c} \mathcal{E}[a] = & \frac{\mathcal{C}}{R} f_1(a/R) - \frac{\mathcal{C}^2}{R^2} f_2(a/R) + \frac{\mathcal{C}^3}{R^3} f_3(a/R) - \frac{\mathcal{D}}{R^3} f_{3,\mathcal{D}}(a/R) - \frac{\mathcal{A}_{00}}{R^3} f_{3,\mathcal{A}_0}(a/R) \\ & - \frac{\mathcal{A}_{11} + \mathcal{A}_{-1-1}}{R^3} f_{3,\mathcal{A}_1}(a/R) - \frac{\mathcal{C}^4}{R^4} f_4(a/R) + \frac{2\mathcal{C}\mathcal{D}}{R^4} f_{4,\mathcal{D}}(a/R) + \frac{\mathcal{C}\mathcal{A}_{00}}{R^4} f_{4,\mathcal{A}}(a/R) \end{aligned} \quad (3.5)$$

where the functions f_i are calculated in terms of modified bessel functions and given in Appendix B.

Next, we examine the accuracy of Eq. (3.5) as compared with the exact prediction of Eq. (3.3). Since we can solve Eq. (3.3) exactly for spheres of all sizes, we compare the two results for various s/R , where $\mathcal{C} = -s$, $\mathcal{D} = -s^3$ and $\mathcal{A}_{mm} = s^3/3$ for the inner sphere. Fig. (3-3) plots the fractional errors $\Delta\mathcal{E} = (\mathcal{E} - \mathcal{E}_{CP})/\mathcal{E}$ as a percentage

versus $x = a/(R - s)$ for various s . \mathcal{E}_{CP} denotes the energy calculated using Eq. (3.5) up to $\mathcal{O}(R^{-3})$. Many trends are visible in this graph, for example the scalar interior Casimir-Polder result through third order differs from the exact result by less than 3 parts in a 100 for all $s/R \leq 0.05$ for $0 < x < 0.6$. Another interesting feature is that for a given value of s/R , $\lim_{x \rightarrow 0} \Delta\mathcal{E}$ appears to be non-zero. Both the exact Casimir energy and the scalar ICP approximation vanish like a^2 as $a \rightarrow 0$ (recall that the value of each at $a = 0$ has been subtracted). Notice, however, that the CP approximation is an expansion in s/R , not a/R , and therefore each term contributes, albeit with smaller magnitude, at $a = 0$.

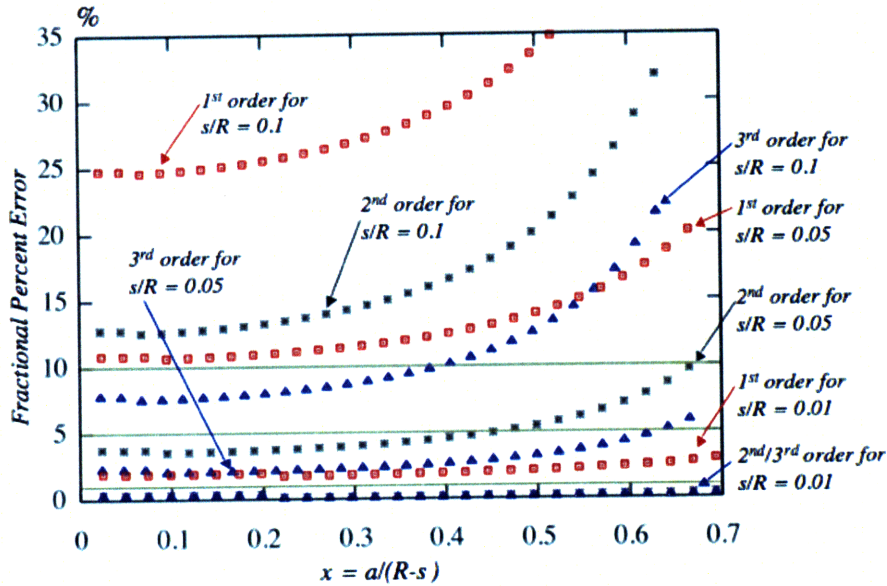


Figure 3-3: Fractional ICP comparison with the exact answer predicted by Eq. (3.3) for a scalar field obeying Dirichlet Boundary Conditions on two spheres in three different configurations: $s/R = 0.1, 0.05, 0.01$. Along the y -axis is the fractional error $(\mathcal{E} - \mathcal{E}_{CP})/\mathcal{E}$ plotted as a percentage, where \mathcal{E}_{CP} is the scalar ICP prediction from Eq. (3.5). For each value of s/R , we have plotted the fractional difference between \mathcal{E} and \mathcal{E}_{CP} at the first three leading orders in Eq. (3.5): $\mathcal{O}(R^{-1})$, $\mathcal{O}(R^{-2})$ and $\mathcal{O}(R^{-3})$. The three gray horizontal lines mark the 10%, 5% and 1% differences.

Chapter 4

Corrections to the PFA

As mentioned in the Introduction, one of the most interesting quantities accessible to us is the first non-trivial correction to the Proximity Force Approximation. In this chapter we extract these corrections for the case of one sphere within another, and combine it with data from the case of two separated spheres and a sphere opposite a plane, to survey the situation over the full range of possible sphere-sphere configurations.

The leading term in the PFA is given by Eq. (1.5) as discussed in the Introduction. The analytic form of the corrections to the PFA is unknown. We find that our data can be fitted very well by the first few terms in a *power series expansion of the Casimir force* in d/s ,

$$\mathcal{F} \sim_{d \rightarrow 0} -\frac{\pi^3 \hbar c}{360 d^3} \frac{sR}{s+R} \left(1 + \theta_1(s/R) \frac{d}{2s} - \theta_2(s/R) \frac{d^2}{2s^2} + \dots \right) \quad (4.1)$$

as $d \rightarrow 0$. A power series expansion of the force requires that the energy include a $\log(d/s)$ term,

$$\mathcal{E} \sim_{d \rightarrow 0} -\frac{\pi^3 \hbar c}{720 d^2} \frac{sR}{s+R} \left(1 + \theta_1(s/R) \frac{d}{s} + \theta_2(s/R) \log \frac{d^2}{s^2} + \alpha(s/R) \frac{d^2}{s^2} + \mathcal{O}\left(\frac{d^3}{s^3}\right) \right) \quad (4.2)$$

where we have adjusted signs in Eq. (4.1) so that the corrections to the PFA energy

in Eq. (4.2) correspond to the extrapolation function $f(d/s)$ defined in Section 2.2. Note that the term proportional to d^2/s^2 in Eq. (4.2) does not contribute to the force. As previously remarked in Sections 2.2 and 3.2, this is the form we have used to fit our numerical results to in order to obtain the first correction, $\theta_1(s/R)$ to the PFA.

It is useful to have an estimate, however crude, of the interior Casimir energy over the whole range of d/R in order to scale out the rapid variation that makes it difficult to display \mathcal{E} graphically. To this end we extend the PFA over the whole range of d , s , and R . The PFA estimate of \mathcal{E} can be calculated by assuming that each interacting surface is assembled out of infinitesimal mirrors spaced at a distance $l(x, y)$ from the other surface, where (x, y) are the coordinates of the surface chosen as a convenient reference. This algorithm is ambiguous beyond the leading term in $1/d$ because there is no unique way to specify the separation between the surfaces. For definiteness, we extend the PFA by taking the distance between the surfaces to be the distance measured radially outward from the smaller sphere and integrate over the surface of the smaller sphere. For reference, see Fig. 4-1. The result, which we refer to as the *full PFA*, is given by,

$$\begin{aligned} \mathcal{E}^{\text{fPFA}} = & -\frac{\pi^3 \hbar c}{720} \left(-\frac{2}{s} + \frac{3(R^2 - a^2)}{as^2} \log \left(\frac{(R+a)(R+s-a)}{(R-a)(R+s+a)} \right) \right. \\ & \left. - \frac{4(R^2 - a^2)}{s((R+s)^2 - a^2)} + \frac{2(R+s)(R^2 - a^2 + s^2)}{((R+s)^2 - a^2)^2} \right) \end{aligned} \quad (4.3)$$

The form that we have used to normalize the Casimir energy in the results displayed in Sections 2.2 and 3.2 can be obtained by substituting $R \rightarrow -R$ in Eq. (4.3). We remind the reader that, in this chapter, $R < 0$ corresponds to the ‘interior’ problem. The full PFA also yields a ‘prediction’ for $\theta_1(s/R)$,

$$\theta_1^{\text{fPFA}}(x) = -x - \frac{x}{1+x} - 3 \quad (4.4)$$

where $x = s/R$. Note that the PFA predicts a smooth continuation from the interior to the exterior problem.

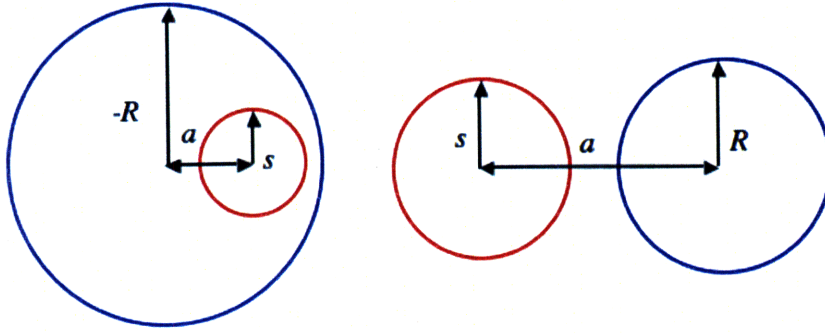


Figure 4-1: On the left side are two spheres of radii s and R where $s < R$. On the right side are two spheres of radii s and R , where the larger sphere's radius is labeled R . The new variable $x = s/R$ defined over the range $-1 < x \leq 1$ covers all sphere-sphere configurations.

We emphasize that there is no reason to expect Eq. 4.4 to provide an accurate representation for the first order correction to the PFA. Nevertheless it provides a result with which we can combine our exact ‘interior’ analysis with the ‘exterior’ analysis of Ref. [2] and the sphere-plane calculation in Ref. [3] to compare $\theta_{1,\text{PFA}}$ with the exact θ_1 . Fig. 4-2 shows such a comparison for $x = s/R = -0.75, -0.6, -0.5, -0.3, 0, 1$, and the numerical values of θ_1 are listed in Table 4.1.

| x | θ_1 | $\Delta\theta_1$ |
|-------|------------|------------------|
| 1.0 | -2.7400 | 0.04000 |
| 0.0 | -1.4100 | 0.02000 |
| -0.3 | -0.5468 | 0.03824 |
| -0.5 | 0.3164 | 0.01400 |
| -0.6 | 0.8483 | 0.01502 |
| -0.75 | 2.6122 | 0.02962 |

Table 4.1: PFA correction coefficients θ_1 for two conducting spheres at various configurations x determined from fitting the exact Casimir energy at small separations d to a function, $\mathcal{E}_{f\text{PFA}}(d/s) = 1 + \theta_1 d/s + \theta_2 \log(d/s)d^2/s^2$. $\Delta\theta_1$ are the fitting errors on our numerical data.

It is evident from Fig. 4-2 that the leading order PFA correction, $\theta_1(x) \sim \theta_1^{\text{PFA}} + 1.8$ to a very good approximation. Thus, we have predicted exact leading order corrections to the PFA for all possible interior and exterior configurations of two conducting spheres.

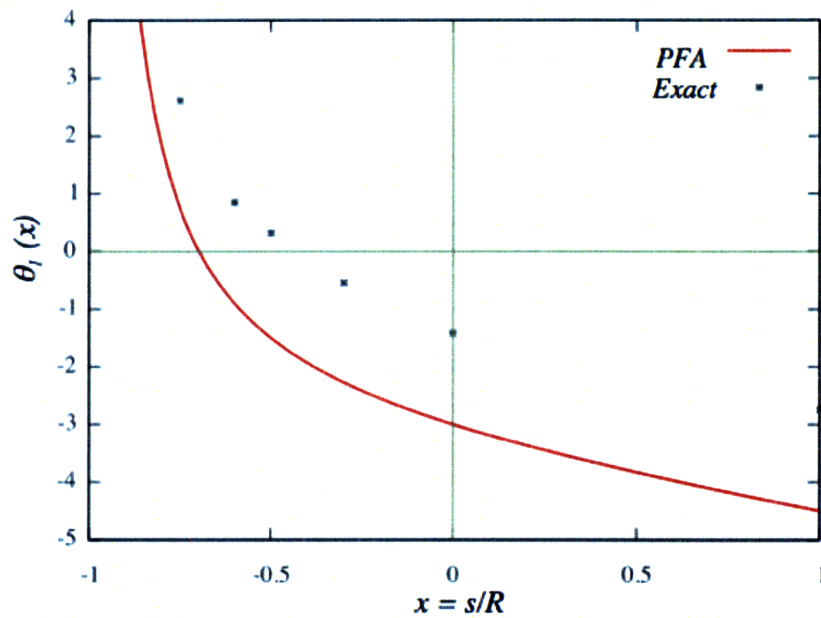


Figure 4-2: PFA correction coefficients for spheres. The x -axis covers the full range of sphere-sphere configurations. $x < 0$ corresponds to the ‘interior’ geometry, $x > 0$ corresponds to the ‘exterior’ geometry and $x = 0$ corresponds to a sphere facing a plane. The red curve is the ‘naive’ prediction of θ_1 from $fPFA$, given in Eq. (4.4). The *Exact* data points correspond to the numerical values listed in Table 4.1. They are calculated using the methods discussed in Section 2.2.

Chapter 5

Conclusions

We have studied the electromagnetic Casimir problem for a metallic compact object contained inside a compact metallic surface. Using the path integral formalism, we express the Casimir energy between the two objects in terms of their *transition* matrices, and *translation* matrices that relate the coordinate systems appropriate to each object. Then we specialize to the case when both objects are conducting spheres, and evaluate the Casimir energy for the specific configuration, $s/R = 0.5$. The Casimir force for this sphere configuration is calculated by numerically differentiating the energy with respect to the spheres' separation.

We have also calculated the analog of the Casimir-Polder expansion for the interior case. When the outer object is a conducting spherical shell, the Casimir energy of the inner object can be expanded as an asymptotic series in s^p/R^p where R is the radius of the outer sphere, and s is a length parameter characterizing the inner object. In the large R limit, the Casimir energy of the inner object is dominated by leading terms in this expansion. We have calculated the coefficient functions for the leading two terms exactly for the case when the inner object is a dielectric sphere. Comparing the interior Casimir-Polder expansion (up to $\mathcal{O}(R^{-5})$) with the exact energy (calculated numerically) for various sphere configurations, we find that the ICP result is accurate to more than 99 parts in a 100 for $a/R \leq 0.3$ through $s/R \leq 0.1$ where a is the displacement of their centers. Therefore, the ICP expansion is exact for a small polarizable object (an atom or a molecule) inside a conducting spherical shell.

The above analysis was repeated for a scalar field obeying Dirichlet or Neumann boundary conditions on spheres inside one another. The ICP expansion for a scalar field obeying Dirichlet boundary conditions on an arbitrary shaped object inside a spherical shell was calculated in a manner analogous to the electromagnetic case.

The methods demonstrated in this paper can be applied very easily to calculate the Casimir force between dielectric spheres at all separations, but they become computationally intensive at close separations of spheres. In this limit, we make contact with the Proximity Force Approximation (PFA). By studying various interior sphere configurations at close separations, we are able to calculate leading order corrections to the PFA. Furthermore, we combine our interior results with previous work on conducting spheres exterior to each other and a conducting sphere facing a mirror to predict leading order PFA corrections for all sphere-sphere configurations.

Appendix A

Casimir Polder Coefficient

Functions: Electromagnetic Field

The interior Casimir Polder coefficient functions can be calculated easily using Eqs. (2.11), (2.17) and (2.18). They are expressed as integrals over the frequency κ in terms of sums of modified bessel functions I_ν and K_ν . Note that we have made the substitutions, $y = a/R$ and $x = \kappa R$ where R is the radius of the conducting spherical shell. The ICP coefficient functions are given as,

$$\begin{aligned}
 f_M(y) = & \int_0^\infty dx x^3 \sum_{l=1}^\infty \left(\frac{K_{l+1/2}(x)}{I_{l+1/2}(x)} \frac{1}{xy} \left((l+1)I_{l-1/2}^2(xy) + lI_{l+3/2}^2(xy) \right) \right. \\
 & \left. - \frac{xy}{2l+1} \left(I_{l-1/2}(xy) - I_{l+3/2}(xy) \right) \frac{2K_{l+1/2}(x) + 2xK'_{l+1/2}(x)}{I_{l+1/2}(x) + 2xI'_{l+1/2}(x)} \right) - \int_0^\infty dx \frac{4x^3}{\pi} \frac{K_{3/2}(x)}{I_{3/2}(x)}
 \end{aligned}
 \tag{A.1}$$

$$\begin{aligned}
 f_E(y) = & \int_0^\infty dx x^3 \sum_{l=1}^\infty \left(\frac{K_{l+1/2}(x) + 2xK'_{l+1/2}(x)}{I_{l+1/2}(x) + 2xI'_{l+1/2}(x)} \frac{1}{xy} \left((l+1)I_{l-1/2}^2(xy) + lI_{l+3/2}^2(xy) \right) \right. \\
 & \left. - \frac{xy}{2l+1} \left(I_{l-1/2}(xy) - I_{l+3/2}(xy) \right) \frac{2K_{l+1/2}(x)}{I_{l+1/2}(x)} \right) - \int_0^\infty dx \frac{4x^3}{\pi} \frac{K_{3/2}(\kappa R) + 2\kappa R K'_{3/2}(\kappa R)}{I_{3/2}(\kappa R) + 2\kappa R I'_{3/2}(\kappa R)}
 \end{aligned}
 \tag{A.2}$$

$$\begin{aligned}
g_M(y) = & \int_0^\infty dx x^5 \left\{ \frac{1}{30xy} \sum_{l=1}^\infty \frac{1}{2l+1} \frac{K_{l+1/2}(x)}{I_{l+1/2}(x)} \left[\frac{15l(l+1)}{2} \left\{ \frac{l-1}{2l-1} I_{l-3/2}(xy) \right. \right. \right. \\
& + \left. \left. \frac{2l+1}{4l(l+1)-3} I_{l+1/2}(xy) - \frac{l+2}{2l+3} I_{l+5/2}(xy) \right\}^2 \right. \\
& + \left. \left. \frac{5}{8} \left\{ \frac{4(l+1)(l-1)}{2l-1} I_{l-3/2}(xy) + \frac{6(2l+1)}{4l(l+1)-3} I_{l+1/2}(xy) + \frac{4l(l+2)}{2l+3} I_{l+5/2}(xy) \right\}^2 \right. \right. \\
& + \left. \left. \frac{5(l-1)(l+2)}{8} \left\{ \frac{2(l+1)}{2l-1} I_{l-3/2}(xy) - \frac{6(2l+1)}{4l(l+1)-3} I_{l+1/2}(xy) - \frac{2l}{2l+3} I_{l+5/2}(xy) \right\}^2 \right] \right. \\
& - \left. \frac{1}{3\pi} \frac{K_{5/2}(x)}{I_{5/2}(x)} - \frac{1}{3} \sum_{l=1}^\infty \frac{xy}{2l+1} \frac{K_{l+1/2}(x) + 2xK'_{l+1/2}(x)}{I_{l+1/2}(x) + 2xI'_{l+1/2}(x)} \right. \\
& \times \left. \left[\frac{1}{4} \left\{ -\frac{l-1}{2l-1} I_{l-3/2}(xy) - \frac{2l-1}{4l(l+1)-3} I_{l+1/2}(xy) + \frac{l+2}{2l+3} I_{l+5/2}(xy) \right\}^2 \right. \right. \\
& + \left. \left. (l-1)(l+2) \left\{ \frac{1}{2(2l-1)} I_{l-3/2}(xy) - \frac{2l+1}{4l(l+1)-3} I_{l+1/2}(xy) + \frac{1}{2(2l+3)} I_{l+5/2}(xy) \right\}^2 \right] \right\} \quad (A.3)
\end{aligned}$$

$$\begin{aligned}
g_E(y) = & \int_0^\infty dx x^5 \left\{ \frac{1}{30xy} \sum_{l=1}^\infty \frac{1}{2l+1} \frac{K_{l+1/2}(x) + 2xK'_{l+1/2}(x)}{I_{l+1/2}(x) + 2xI'_{l+1/2}(x)} \left[\frac{15l(l+1)}{2} \left\{ \frac{l-1}{2l-1} I_{l-3/2}(xy) \right. \right. \right. \\
& + \left. \left. \frac{2l+1}{4l(l+1)-3} I_{l+1/2}(xy) - \frac{l+2}{2l+3} I_{l+5/2}(xy) \right\}^2 \right. \\
& + \left. \left. \frac{5}{8} \left\{ \frac{4(l+1)(l-1)}{2l-1} I_{l-3/2}(xy) + \frac{6(2l+1)}{4l(l+1)-3} I_{l+1/2}(xy) + \frac{4l(l+2)}{2l+3} I_{l+5/2}(xy) \right\}^2 \right. \right. \\
& + \left. \left. \frac{5(l-1)(l+2)}{8} \left\{ \frac{2(l+1)}{2l-1} I_{l-3/2}(xy) - \frac{6(2l+1)}{4l(l+1)-3} I_{l+1/2}(xy) - \frac{2l}{2l+3} I_{l+5/2}(xy) \right\}^2 \right] \right. \\
& - \left. \frac{1}{3\pi} \frac{K_{5/2}(x) + 2xK'_{5/2}(x)}{I_{5/2}(x) + 2xI'_{5/2}(x)} - \frac{1}{3} \sum_{l=1}^\infty \frac{xy}{2l+1} \frac{K_{l+1/2}(x)}{I_{l+1/2}(x)} \left[\frac{1}{4} \left\{ -\frac{l-1}{2l-1} I_{l-3/2}(xy) \right. \right. \right. \\
& - \left. \left. \frac{2l-1}{4l(l+1)-3} I_{l+1/2}(xy) + \frac{l+2}{2l+3} I_{l+5/2}(xy) \right\}^2 \right. \\
& + \left. \left. (l-1)(l+2) \left\{ \frac{1}{2(2l-1)} I_{l-3/2}(xy) - \frac{2l+1}{4l(l+1)-3} I_{l+1/2}(xy) + \frac{1}{2(2l+3)} I_{l+5/2}(xy) \right\}^2 \right] \right\} \quad (A.4)
\end{aligned}$$

Appendix B

Casimir Polder Coefficient Functions: Scalar Field

The interior Casimir Polder coefficient functions for a scalar field obeying Dirichlet boundary conditions can be calculated easily using Eqs. (3.1), (3.2) and (3.4). They are expressed as integrals over the frequency κ in terms of sums of modified Bessel functions I_ν and K_ν . Again, we make the substitutions $y = a/R$ and $x = \kappa R$ where R is the radius of the conducting spherical shell. The scalar ICP coefficient functions are given as,

$$f_1(y) = \int_0^\infty dx x \left\{ \sum_l \frac{2l+1}{xy} \frac{K_{l+1/2}(x)}{I_{l+1/2}(x)} I_{l+1/2}^2(xy) - \frac{2}{\pi} \frac{K_{1/2}(x)}{I_{1/2}(x)} \right\} \quad (\text{B.1})$$

$$f_2(y) = \int_0^\infty dx x^2 \left\{ \sum_l \frac{2l+1}{xy} \frac{K_{l+1/2}(x)}{I_{l+1/2}(x)} I_{l+1/2}^2(xy) - \frac{2}{\pi} \frac{K_{1/2}(x)}{I_{1/2}(x)} \right\} \\ + \int_0^\infty dx x^2 \left\{ \sum_{l,\mu} \frac{(2l+1)(2\mu+1)}{2x^2y^2} \frac{K_{l+1/2}(x)}{I_{l+1/2}(x)} \frac{K_{\mu+1/2}(x)}{I_{\mu+1/2}(x)} I_{l+1/2}^2(xy) I_{\mu+1/2}^2(xy) - \frac{2}{\pi^2} \frac{K_{1/2}^2(x)}{I_{1/2}^2(x)} \right\} \quad (\text{B.2})$$

$$\begin{aligned}
f_3(y) &= \int_0^\infty dx x^3 \left\{ \sum_l \frac{2l+1}{xy} \frac{K_{l+1/2}(x)}{I_{l+1/2}(x)} I_{l+1/2}^2(xy) - \frac{2}{\pi} \frac{K_{1/2}(x)}{I_{1/2}(x)} \right\} \\
&+ \int_0^\infty dx 2x^3 \left\{ \sum_{l,\mu} \frac{(2l+1)(2\mu+1)}{2x^2y^2} \frac{K_{l+1/2}(x)}{I_{l+1/2}(x)} \frac{K_{\mu+1/2}(x)}{I_{\mu+1/2}(x)} I_{l+1/2}^2(xy) I_{\mu+1/2}^2(xy) - \frac{2}{\pi^2} \frac{K_{1/2}^2(x)}{I_{1/2}^2(x)} \right\} \\
&+ \int_0^\infty dx \left\{ \sum_{\lambda,\mu,\nu} \frac{1}{3y^3} \left(\prod_{l=\lambda,\mu,\nu} (2l+1) \frac{K_{l+1/2}(x)}{I_{l+1/2}(x)} I_{l+1/2}^2(xy) \right) - \frac{8x^3}{3\pi^3} \frac{K_{1/2}^3(x)}{I_{1/2}^3(x)} \right\}
\end{aligned} \tag{B.3}$$

$$f_{3,\mathcal{D}}(y) = \int_0^\infty dx x^3 \left\{ \sum_l \frac{2l+1}{xy} \frac{K_{l+1/2}(x)}{I_{l+1/2}(x)} I_{l+1/2}^2(xy) - \frac{2}{\pi} \frac{K_{1/2}(x)}{I_{1/2}(x)} \right\} \tag{B.4}$$

$$f_{3,\mathcal{A}_0}(y) = \int_0^\infty dx x^3 \left\{ \sum_l \frac{1}{xy(2l+1)} \frac{K_{l+1/2}(x)}{I_{l+1/2}(x)} [(l+1)I_{l+3/2}(xy) + lI_{l-1/2}(xy)]^2 - \frac{2}{3\pi} \frac{K_{3/2}(x)}{I_{3/2}(x)} \right\} \tag{B.5}$$

$$f_{3,\mathcal{A}_1}(y) = \int_0^\infty dx x^3 \left\{ \sum_l \frac{l(l+1)}{2xy(2l+1)} \frac{K_{l+1/2}(x)}{I_{l+1/2}(x)} [I_{l+3/2}(xy) - I_{l-1/2}(xy)]^2 - \frac{2}{3\pi} \frac{K_{3/2}(x)}{I_{3/2}(x)} \right\} \tag{B.6}$$

$$\begin{aligned}
f_4(y) &= \int_0^\infty dx x^4 \left\{ \sum_l \frac{2l+1}{xy} \frac{K_{l+1/2}(x)}{I_{l+1/2}(x)} I_{l+1/2}^2(xy) - \frac{2}{\pi} \frac{K_{1/2}(x)}{I_{1/2}(x)} \right\} \\
&+ \int_0^\infty dx 3x^4 \left\{ \sum_{l,\mu} \frac{(2l+1)(2\mu+1)}{2x^2y^2} \frac{K_{l+1/2}(x)}{I_{l+1/2}(x)} \frac{K_{\mu+1/2}(x)}{I_{\mu+1/2}(x)} I_{l+1/2}^2(xy) I_{\mu+1/2}^2(xy) - \frac{2}{\pi^2} \frac{K_{1/2}^2(x)}{I_{1/2}^2(x)} \right\} \\
&+ \int_0^\infty dx \left\{ \frac{x}{y^3} \sum_{\lambda,\mu,\nu} \left(\prod_{l=\lambda,\mu,\nu} (2l+1) \frac{K_{l+1/2}(x)}{I_{l+1/2}(x)} I_{l+1/2}^2(xy) \right) - \frac{8x^4}{\pi^3} \frac{K_{1/2}^3(x)}{I_{1/2}^3(x)} \right\} \\
&+ \int_0^\infty dx \left\{ \sum_{\lambda,\mu,\nu,\sigma} \frac{1}{4y^4} \left(\prod_{l=\lambda,\mu,\nu,\sigma} (2l+1) \frac{K_{l+1/2}(x)}{I_{l+1/2}(x)} I_{l+1/2}^2(xy) \right) - \frac{4x^4}{\pi^4} \frac{K_{1/2}^4(x)}{I_{1/2}^4(x)} \right\}
\end{aligned} \tag{B.7}$$

$$\begin{aligned}
f_{4,\mathcal{D}}(y) &= \int_0^\infty dx x^4 \left\{ \sum_l \frac{2l+1}{xy} \frac{K_{l+1/2}(x)}{I_{l+1/2}(x)} I_{l+1/2}^2(xy) - \frac{2}{\pi} \frac{K_{1/2}(x)}{I_{1/2}(x)} \right\} \\
&+ \int_0^\infty dx x^4 \left\{ \sum_{l,\mu} \frac{(2l+1)(2\mu+1)}{2x^2y^2} \frac{K_{l+1/2}(x)}{I_{l+1/2}(x)} \frac{K_{\mu+1/2}(x)}{I_{\mu+1/2}(x)} I_{l+1/2}^2(xy) I_{\mu+1/2}^2(xy) - \frac{2}{\pi^2} \frac{K_{1/2}^2(x)}{I_{1/2}^2(x)} \right\}
\end{aligned} \tag{B.8}$$

$$\begin{aligned}
f_{4,\mathcal{A}}(y) &= \int_0^\infty dx \left\{ \sum_{l,\mu} \frac{x^2}{y^2} \frac{K_{l+1/2}(x)}{I_{l+1/2}(x)} \frac{K_{\mu+1/2}(x)}{I_{\mu+1/2}(x)} I_{l+1/2}(xy) I_{\mu+1/2}(xy) [(l+1)I_{l+3/2}(xy) + lI_{l-1/2}(xy)] \right. \\
&\quad \left. \times [(\mu+1)I_{\mu+3/2}(xy) + \mu I_{\mu-1/2}(xy)] \right\}
\end{aligned} \tag{B.9}$$

Bibliography

- [1] H. B. G. Casimir, *Indag. Math.* **10**, 261 (1948) [*Kon. Ned. Akad. Wetensch. Proc.* **51**, 793 (1948)]
- [2] T. Emig, N. Graham, R. L. Jaffe, and M. Kardar, *Phys. Rev. Lett.* **99**, 170403 (2007);
- [3] T Emig *J. Stat. Mech.* (2008) P04007
- [4] See for example, S. Reynaud, P. A. Maia Neto and A. Lambrecht (2008). *Journal of Physics A: Mathematical and Theoretical*, **41**, pp. 164004, M. Bordag and V. Nikolaev (April 2008). *Journal of Physics A: Mathematical and Theoretical*, **41**, pp. 164002, and D. E. Krause, R. S. Decca, D. Lopez, and E. Fischbach, *Phys. Rev. Lett.* **98**, 050403 (2007), DOI:10.1103/PhysRevLett.98.050403
- [5] D. A. R. Dalvit, F. C. Lombardo, F. D. Mazzitelli, and R. Onofrio, *Phys. Rev. A* **74**, 020101(R) (2006)
- [6] Valery N. Marachevsky, *Phys. Rev. D* **75**, 085019 (2007)
- [7] S. J. Rahi, T. Emig, N. Graham, R. L. Jaffe, M. Kardar, in preparation.
- [8] O. Kenneth and I. Klich, *Phys. Rev. B* **78**, 014103 (2008).
- [9] T. Emig, N. Graham, R. L. Jaffe, and M. Kardar, *Phys. Rev. D* **77**, 025005 (2008).
- [10] S. J. Rahi, T. Emig, R. L. Jaffe, and M. Kardar. arXiv:0805.4241v1 [cond-mat.stat-mech](2008)
- [11] H. Li and M. Kardar, *Phys. Rev. Lett.* **67**, 3275 (1991); *Phys. Rev. A* **46**, 6490 (1992)
- [12] T. Emig, N. Graham, R. L. Jaffe, and M. Kardar. arXiv:0811.1597v1 [cond-mat.stat-mech]
- [13] H. B. G. Casimir and D. Polder, *Phys. Rev.* **73**, 360 (1948).
- [14] B. V. Derjagin, *Kolloid Z.* **69** 155 (1934), B. V. Derjagin, I. I. Abriksova, and E. M. Lifshitz, *Sov. Phys. JETP* **3**, 819 (1957); For a modern discussion of the Proximity Force Theorem, see J. Blocki and W. J. Swiatecki, *Annals Phys.* **132**, 53 (1981)

- [15] A. Scardicchio and R. L. Jaffe. Nuclear Physics B 704 [FS] (2005) 552-582, arXiv: quant-ph/0406041 (June 2004)
- [16] M. Schaden and L. Spruch, Phys. Rev. A **58**, 935 (1998).
- [17] R. C. Wittmann, IEEE Transactions on Antennas and Propagation, **36**, 1078 (1988)
- [18] M. Bordag, D. Robashik, and E. Wieczorek, Ann. Phys. **165**, 192 (1985)
- [19] J. M. Blatt and V. F. Weisskopf. Chapter 3 in *Theoretical Nuclear Physics*, John Wiley & Sons, New York.